 Open access • Journal Article • DOI:10.1021/ACSEARTHSPACECHEM.0C00231

High-Temperature Thermodynamics of Cerium Silicates, A-Ce₂Si₂O₇, and Ce_{4.67}(SiO₄)₃O — Source link

Andrew C. Strzelecki, Kyle W. Kriegsman, Paul Estevenon, Vitaliy G. Goncharov ...+7 more authors

Institutions: Washington State University, Centre national de la recherche scientifique, Brookhaven National Laboratory

Published on: 30 Oct 2020

Topics: Calorimetry, Thermal decomposition, Differential scanning calorimetry, Standard enthalpy of formation and Thermogravimetric analysis

Related papers:

- [Contribution to phase equilibria in the Ce₂O₃ rich part of the Ce₂O₃-SiO₂-ZrO₂ system](#)
- [High temperature reactions between Ce₂O₃ and Al₂O₃, and the properties of the cerium aluminates formed](#)
- [Phase Stability and Thermophysical Properties of Neodymium Cerium Composite Oxide.](#)
- [Study on properties of the single-phase cubic Ce_{0.5}Zr_{0.5}O₂ solid solution](#)
- [Influence of synthesis conditions on the crystal structure of the powder formed in the “HfO₂ - CeO₂ /Ce₂O₃” system](#)

Share this paper:    

View more about this paper here: <https://typeset.io/papers/high-temperature-thermodynamics-of-cerium-silicates-a-1lc5iygr5b>

High temperature thermodynamics of Cerium Silicates, $A\text{-Ce}_2\text{Si}_2\text{O}_7$, and $\text{Ce}_{4.67}(\text{SiO}_4)_3\text{O}$

Andrew C. Strzelecki^{1,2,3}, Kyle Kriegsman^{1,2}, Paul Estevenon^{4,5}, Vitaliy Goncharov^{1,2,3}, Jianming Bai⁶, Stephanie Szenknect⁴, Adel Mesbah⁴, Di Wu^{1,2,3,7}, John S. McCloy^{1,3,8}, Nicolas Dacheux⁴, Xiaofeng Guo^{1,2,3*}

¹ *Department of Chemistry, Washington State University, Pullman, Washington 99164, United States*

² *Alexandra Navrotsky Institute for Experimental Thermodynamics, Washington State University, Pullman, Washington 99164, United States*

³ *Materials Science and Engineering, Washington State University, Pullman, Washington 99164, United States*

⁴ *ICSM, Univ Montpellier, CNRS, CEA, ENSCM, Site de Marcoule, Bagnols sur Cèze, France*

⁵ *CEA, DES, ISEC, DMRC, Univ Montpellier, Marcoule, France*

⁶ *National Synchrotron Light Source II, Brookhaven National Laboratory, Upton, New York 11973, United States*

⁷ *The Gene and Linda Voiland School of Chemical Engineering and Bioengineering, Washington State University, Pullman, Washington 99164, United States*

⁸ *School of Mechanical and Materials Engineering, Washington State University, Pullman, Washington 99164, United States*

* e-mail: x.guo@wsu.edu

To be submitted to *ACS Earth and Space Chemistry*

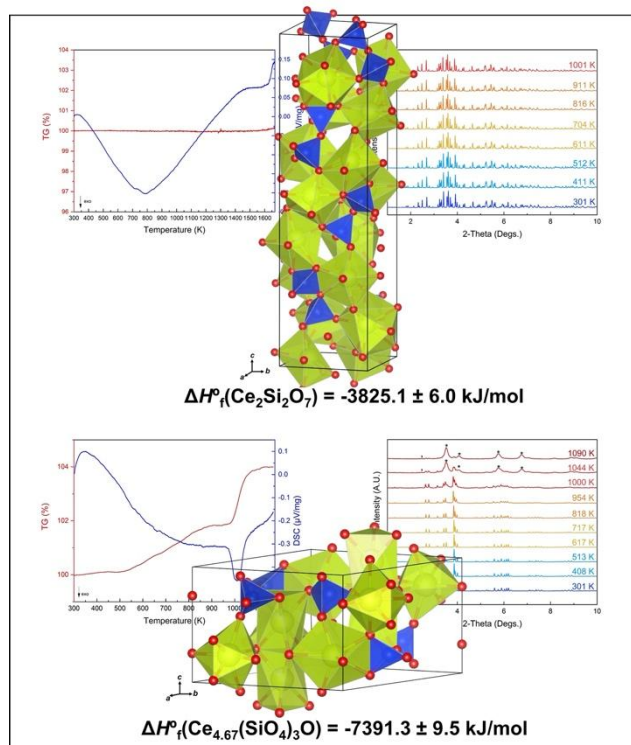
August 2020

Abstract:

Lanthanide disilicates and oxyapatites have potential roles in high temperature applications as thermal (TBC) and environmental barrier coatings (EBC), or possible alteration phases in geological nuclear waste repositories. However, those Ce³⁺-bearing silicates have only been limitedly studied. In this work we performed detailed structural and thermodynamic investigations on A-Ce₂Si₂O₇ (tetragonal, *P4₁*) and Ce_{4.67}(SiO₄)₃O (hexagonal, *P6₃/m*). The high temperature structural behaviors and coefficients of thermal expansion were determined by *in situ* high temperature synchrotron X-ray diffraction (HT-XRD) implemented with Rietveld analysis and thermogravimetric analysis coupled with differential scanning calorimetry (TGA-DSC). A-Ce₂Si₂O₇ was found to be stable in N₂ and air up to ~1483 K with an isotropic thermal expansion ($\alpha_a = 12.3 \times 10^{-6} \text{ K}^{-1}$ and $\alpha_c = 12.4 \times 10^{-6} \text{ K}^{-1}$). Ce_{4.67}(SiO₄)₃O had a slow partial oxidation between 533 K and 873 K to a new nonstoichiometric phase Ce³⁺_{1.67-x}Ce⁴⁺_xCe³⁺₃(SiO₄)₃O_{1+0.5x}, followed by a thermal decomposition to CeO₂ and SiO₂ at ~1000 K. By using high temperature oxide melt solution calorimetry at 973 K with lead borate as solvent, we determined, for the first time, the standard enthalpy of formation of A-Ce₂Si₂O₇ (-3825.1 ± 6.0 kJ/mol) and Ce_{4.67}(SiO₄)₃O (-7391.3 ± 9.5 kJ/mol). These thermodynamic parameters were compared with those of CeO₂, CeSiO₄, and other silicate oxyapatites for examining their chemical stability in high temperature environments relevant for aeronautical applications, mineral formation, and nuclear fuel cycle.

Keywords: cerium sorosilicate; cerium oxyapatite; thermodynamics; enthalpy of formation; thermal barrier coating; environmental barrier coatings; ceramic waste forms; rare earth minerals; lanthanide geochemistry

Highlights:



1. Introduction:

Rare-earth disilicates ($\text{RE}_2\text{Si}_2\text{O}_7$) display the largest number of polymorphs of any rare earth-earh oxide compounds¹, and have applications as thermal (TBCs) and environmental barrier coatings (EBCs) for ceramic matrix composite materials (CMC), such as silicon carbide (SiC) or molybdenum disilicide (MoSi_2).¹⁻³ The advantages of silicate-based coating materials are their high thermal stability and resistance to oxidation, while possessing congruent coefficients of thermal expansion (CTE) with the existing high temperature CMC (Table 1).^{1,2,4-9} This makes the rare-earth disilicates an attractive potential candidates to be used in high temperature combustion engines for aerospace applications which are to replace traditional nickel based super alloys.^{2,3} However, during the take-off and landing of aircraft, various rare-earth oxyapatites ($\text{M}^{2+}\text{RE}_4(\text{SiO}_4)_3\text{O}$) are known to form as corrosion products between the rare-earth disilicates EBC and molten aerosol mineral dust, composed primarily of $\text{CaO-MgO-Al}_2\text{O}_3\text{-SiO}_2$ (CMAS).^{10,11} Such rare-earth oxyapatite corrosion products are thermodynamically stable and can serve as an effective passivating layer to reduce or prevent further pitting and erosion of EBC/CMC on the engines of the aircraft.^{10,12,13} Conversely, the potential mismatch of CTEs of the rare-earth oxyapatite and the EBC/CMC could also cause increased internal stresses to build promoting mechanical failure.

In addition to their high temperature properties, these rare earth silicates material families have potential applications to various other fields and technologies due to their diverse properties originating from the $4f$ electronic states.¹⁴⁻¹⁶ Examples of such applications include use as scintillators and detectors in monitoring radionuclides¹⁷⁻¹⁹; ion-exchange medium for the separation of radionuclides owing to their efficient ability for ion exchange and robust nature²⁰; and optoelectronics (lasers and optical fibers) as a result of the thermal stability of

their optical transmission.^{17,18,21} As a result, structural and thermochemical investigations have been detailed at both low and high temperatures.^{1,2,21-27,11,14-20} However, the thermophysical and thermochemical understanding of the low temperature polymorph of cerium disilicate (A-Ce₂Si₂O₇; space group *P4₁*) and the cation-vacant cerium oxyapatite (Ce_{4.67}(SiO₄)₃O; space group *P6₃/m*) are still largely absent (Figure 1). Additionally, as Ce is the most abundant rare earth element²⁸ and an effective surrogate for Pu in the solid state system,²⁹⁻³³ the thermodynamic properties of A-Ce₂Si₂O₇ and Ce_{4.67}(SiO₄)₃O are fundamentally needed for geochemical modeling and desirable for helping evaluate the thermodynamics of Pu in silicate solid systems.

Indeed, both of the Ce(III) silicates widely exist in natural systems, industrial processing, and synthetic conditions. A-Ce₂Si₂O₇ is found in nature as the mineral percleveite³⁴ and Ce_{4.67}(SiO₄)₃O in the manufacturing of steel.^{26,35} Ce_{4.67}(SiO₄)₃O also belongs to cation-vacant rare earth oxyapatites, an important family among the rare earth silicates as they can crystalize all 17 rare earth elements (Sc, Y, La-Lu).^{15,21} Furthermore, in the pursuit of pure cerium orthosilicate (CeSiO₄; space group *I4₁/amd*), a rare mineral,³⁶ which is isostructural to coffinite (USiO₄), thorite (ThSiO₄), and PuSiO₄, both A-Ce₂Si₂O₇ and Ce_{4.67}(SiO₄)₃O were used as solid precursors during hydrothermal synthesis.³⁷ Such observations imply that the three Ce silicate phases could be close in energetics. A recent work published by Estevenon *et al.*³⁸ in 2020 also showed that impure PuSiO₄ was synthesized hydrothermally from a plutonium disilicate (Pu₂Si₂O₇) precursor, again suggesting the equilibrium between these silicate phases. Such a closeness in energetics could be detrimental for nuclear waste applications. In the permanent disposal of nuclear wastes, either in a deep bore-hole or mined geologic repository, elevated temperatures (343–623 K) will be encountered by the waste forms as a result of both the radiogenic heat mainly generated from the beta decay of short lived radionuclides and also the geothermal gradient.³⁹⁻⁴³ These elevated conditions imitate natural metasomatic conditions within hydrothermal ore deposits.⁴⁴ Radionuclides, especially actinides (An), when leaked from the multi-barrier systems, may interact with silicate-rich fluids. They could potentially form An-silicate colloids,⁴⁵⁻⁴⁸ solid particles,^{38,49,50} or An-silicate aqueous complexes^{51,52} under either hydrothermal conditions presented in the early stages of the repository or ambient conditions in either the late stages of the repository or down the hydrogeological gradient. Such concerns are further justified as it has been previously demonstrated that Pu and other actinides, can be transported on immense distances in the colloidal forms.⁵³⁻⁵⁵

Thus, studying the thermodynamic properties and high temperature thermal stability of these two cerium silicate materials has both fundamental and applicable significance. In this work, we performed structural and calorimetric investigations on A-Ce₂Si₂O₇ and Ce_{4.67}(SiO₄)₃O by thermogravimetric analysis coupled with differential scanning calorimetry (TGA-DSC), *in situ* high temperature synchrotron X-ray diffraction (HT-XRD) and high temperature oxide melt drop solution calorimetry. The determined CTEs and enthalpies of formation (ΔH_f) enable us to further evaluate their high temperature thermochemical reactions and thermophysical behaviors relevant to high temperature material science applications, geochemical associations of these materials, and the nuclear fuel cycle.

2. Experimental Methods

2.1. Sample synthesis and characterization:

All the reagents used for synthesis were of analytical grade. The acid and base solutions used for the experiments include nitric, hydrochloric and sulfuric acids solutions prepared by dilution of ACS grade solutions: HNO_3 (70%), HCl (37%) and H_2SO_4 (95–98 %), and $8 \text{ mol}\cdot\text{L}^{-1}$ NaOH solution freshly prepared from ACS grade NaOH (98 %). The two cerium (III) silicates, $\text{A-Ce}_2\text{Si}_2\text{O}_7$ and $\text{Ce}_{4.67}(\text{SiO}_4)_3\text{O}$, were both prepared via solid state synthetic techniques. This involved mixing of well-milled CeO_2 (99.5%) and SiO_2 (99.5%) in a stoichiometric proportion to the target materials, then pelletizing the homogenous powder under 5 MPa at room temperature. Following this, the pelletized samples were heated to 1623 K for 9 hours under $\text{Ar} - \text{H}_2$ 4% atmosphere in order to guarantee the reduction of cerium. Thorough phase identification was accomplished by powder X-ray diffraction (PXRD), Raman spectroscopy, and infrared spectroscopy. A more detailed description of the synthesis procedure and characterization techniques is described in the previously published work.³⁷

2.2. Thermogravimetric analysis coupled with differential scanning calorimetry (TGA-DSC):

The TGA-DSC measurements were performed on a Setaram SetSYS thermogravimetric differential scanning calorimeter, where $\text{Ce}_{4.67}(\text{SiO}_4)_3\text{O}$ and $\text{A-Ce}_2\text{Si}_2\text{O}_7$ were heated from 301 K to 1473 K and from 301 K to 1673 K, respectively, with a heating rate of 10 K/minute, under a flowing N_2 atmosphere (20 mL/min). In addition, each compound was also heated from 301 K to 1273 K with a heating rate of 10 K/minute under a flowing standard air atmosphere (20 mL/min). The temperature and sensitivity of the instrument was calibrated by heating indium, tin, lead, zinc, and aluminum across their fusion point repeatedly at the temperature change rates of 5, 10, 15, and 20 K/min. The signal of each phase transition was then calibrated against the known heats of fusion for the metals.

2.3. In situ High temperature powder X-ray diffraction (HT-PXRD):

In situ HT-PXRD was conducted at the Sector 28-ID-2 of National Synchrotron Light Source-II (NSLS-II) at Brookhaven National Laboratory. The wavelength of the X-ray beam was 0.1949 Å (63.6 keV), with a beam size of 0.60×0.20 mm. $\text{A-Ce}_2\text{Si}_2\text{O}_7$ and $\text{Ce}_{4.67}(\text{SiO}_4)_3\text{O}$ powders were contained in a silica glass capillary (1 mm ID, 0.25 mm thickness) with one side opened to the air. The capillary was then inserted into a custom-built, Kanthal coil based furnace under standard atmosphere for heating and cooling. A K-type thermocouple was mounted near the center of the heating coil and was used to monitor and to control the temperature. The sample temperature was calibrated by measuring the CTE of a standard ceria powder at different temperature points, with a heating rate of 20 K/min. The data was collected every 50 K during heating and every 200 K during cooling, from room temperature up to 1052 K. Approximately 3

mins of idle time was achieved between reaching the temperature points and data collection in order to establish thermal equilibrium. All collected two-dimensional images (2D) were calibrated, masked, and integrated through the use of Dioptas processing software.⁵⁶ The obtained diffraction patterns were then analyzed through Rietveld method using General Structure Analysis System software version II (GSAS-II),⁵⁷ where the instrument parameters were obtained using the CeO₂ standard. The backgrounds of A-Ce₂Si₂O₇ and Ce_{4.67}(SiO₄)₃O were modelled by the Chebyshev function with 12 coefficients. The starting points of the refinements was the structure reported by Deng and Ibers⁵⁸ for A-Ce₂Si₂O₇ and the structure reported by Belokoneva *et al.*⁵⁹ for Ce_{4.67}(SiO₄)₃O. The resulting refinements yielded R_{wp} values ranging from 2.18 to 5.38 % for A-Ce₂Si₂O₇ and 3.92 to 8.58 % for Ce_{4.67}(SiO₄)₃O. Representative patterns resulting from the fitting are shown in Figures 2 and 3, for A-Ce₂Si₂O₇ and Ce_{4.67}(SiO₄)₃O, respectively. The refined unit cell parameters of A-Ce₂Si₂O₇ and Ce_{4.67}(SiO₄)₃O are listed in Tables 2 and 3 and exhibited in Figures 4 and 5, respectively.

2.4. High temperature oxide melt drop solution calorimetry:

The enthalpies of drop solution (ΔH_{ds}) were directly measured by a Setaram AlexSYS-1000 Calvet-type calorimeter. The calibration of the instrument was conducted by performing transpose temperature drops using solid pieces of α -Al₂O₃ (36-50 mg) and Pt (160-230 mg). Powdered samples were hand-pressed into pellets, with a mass of 3.5-6.6 mg, and dropped from room temperature into a molten solvent of lead borate (2PbO·B₂O₃) contained in a Pt crucible at 973 K under flowing compressed air with a rate of 100 mL/min. While it is known that the sodium molybdate (3Na₂O·4MoO₃) solvent can readily dissolve lanthanides better than PbO·B₂O₃ at 973 K, it is chemically inert to Si.⁶⁰ Therefore, the lead borate solvent was chosen to be used in this work. All of the calibration and methodology employed in this study were further described previously in more details.⁶⁰⁻⁶⁶

3. Results

3.1. Thermogravimetric analysis coupled with differential thermal analysis (TGA-DSC):

From the TGA-DSC result under an inert N₂ atmosphere, A-Ce₂Si₂O₇ showed no apparent mass loss over the entire temperature regime (301–1673 K, Figure 6). However, a change in the heat flow was observed from 1483 to 1583 K. This change in the heat flow is interpreted as the isochemical phase change from the low temperature tetragonal, $P4_1$, A-phase to the high-temperature monoclinic, $P2_1/n$, G-phase.^{27,37,67} Such transition involves the reconstruction of the coordination polyhedra, through breaking of the cerium-oxygen bonds¹⁶ and is consistent with previously reported findings of being a “sluggish” transition from 1523 K to 1548 K.^{27,67} The TGA-DSC result of Ce_{4.67}(SiO₄)₃O exhibited no mass loss or phase transition from 301 K to 1473 K (Figure 7), which is also in good agreement with the previous study

showing that $\text{Ce}_{4.67}(\text{SiO}_4)_3\text{O}$ was found to be stable under N_2 atmosphere up to its melting point of 2143 K.²⁷

Under an oxidative atmosphere (synthetic air), $\text{A-Ce}_2\text{Si}_2\text{O}_7$ had a similar thermal stability (Figure 8), with no signs of degradation or polymorphism, while $\text{Ce}_{4.67}(\text{SiO}_4)_3\text{O}$ was found to be unstable, as suggested by two weight gains (Figure 9). The first mass gain of 1.66% occurred from 533 K to 923 K. It was associated with the oxidation of Ce^{3+} to Ce^{4+} , resulting in a cerium oxyapatite of mixed valence states with a proposed chemical formula $\text{Ce}^{3+}_{1.67-x}\text{Ce}^{4+}_x\text{Ce}^{3+}_3(\text{SiO}_4)_3\text{O}_{1+0.5x}$. The second mass gain of 2.10% occurred between 973 K and 1123 K. It was attributed to the decomposition of $\text{Ce}^{3+}_{1.67-x}\text{Ce}^{4+}_x\text{Ce}^{3+}_3(\text{SiO}_4)_3\text{O}_{1+0.5x}$ into its binary oxides, SiO_2 and CeO_2 . These conclusions are further supported by the following HT-XRD results as reported below.

3.2. In situ High temperature X-ray Diffraction (HT-XRD) of $\text{A-Ce}_2\text{Si}_2\text{O}_7$

Figure S1 shows the temperature dependent XRD patterns of $\text{A-Ce}_2\text{Si}_2\text{O}_7$ in the temperature range between 301 K and 1052 K in air atmosphere. The absence of phase decomposition or transition is consistent with our TGA-DSC experiment performed in air (Figure 8) and previous studies.^{27,37,67} Rietveld analysis of the XRD data allowed to determine the variation of the unit cell parameters as a function of temperature. The linear regressions of such data along both the a -axes and the c -axes (Figure 4) yielded:

$$301 - 1052 \text{ K} \quad a \text{ (\AA)} = 6.7727 + 8.32 \times 10^{-5}T \quad R^2 = 0.998 \quad (1)$$

$$301 - 1052 \text{ K} \quad c \text{ (\AA)} = 24.637 + 30.7 \times 10^{-5}T \quad R^2 = 0.998 \quad (2)$$

The derived mean CTEs of $\text{A-Ce}_2\text{Si}_2\text{O}_7$ are: $\alpha_a = 12.3 \times 10^{-6} \text{ K}^{-1}$ and $\alpha_c = 12.4 \times 10^{-6} \text{ K}^{-1}$, suggesting that $\text{Ce}_2\text{Si}_2\text{O}_7$ has a near isotropic thermal expansion ($\alpha_c/\alpha_a = 1.01$). This isotropic expansion is consistent with the thermal behavior of an isostructural sorosilicate, $\text{A-Nd}_2\text{Si}_2\text{O}_7$ ¹.

3.3. in situ High temperature X-ray Diffraction (HT-XRD) of $\text{Ce}_{4.67}(\text{SiO}_4)_3\text{O}$

The Rietveld refinement of HT-XRD data of $\text{Ce}_{4.67}(\text{SiO}_4)_3\text{O}$ (Figure S2) are in excellent agreement with the TGA-DSC analysis under standard air atmosphere. Above 1004 K, $\text{Ce}_{4.67}(\text{SiO}_4)_3\text{O}$ decomposed into a mixture of CeO_2 and SiO_2 (Figures 5b and S2), corresponding to the second mass gain from 973 K to 1073 K found in the TGA-DSC analysis (Figure 9). Between 559 K and 668 K, although there was no obvious structural change from space group $P6_3/m$, the parameter c decreased to the opposite of thermal expansion (Figure 5), which was discontinued from those before 559 K and after 668 K. This can be attributed to the gradual oxidation of Ce^{3+} (1.196 Å)⁶⁸ to the smaller Ce^{4+} (1.01 Å) in the nine-coordination environment by incorporating additional “free oxygen”²¹ in the special positions (0, 0, ¼) and (0, 0, ¾). This led to an increasing Ce^{4+} content in a chemically changing and non-stoichiometric phase of $\text{Ce}^{3+}_{1.67-x}\text{Ce}^{4+}_x\text{Ce}^{3+}_3(\text{SiO}_4)_3\text{O}_{1+0.5x}$ ($0 < x < 0.27$). Specifically, $\text{Ce}_{4.67}(\text{SiO}_4)_3\text{O}$ possesses two CeO_9 face-sharing polyhedra along the c -axis in the unit cell, which is mainly impacted by the reduction in size from Ce^{3+} to

Ce⁴⁺ by ~15%. An overall shrinkage along the CeO₉ polyhedral chains was found to be 0.14% at 559 K, which corresponds to approximately 1% of Ce atoms being oxidized. The lattice expansion along the *a* axis is nearly linear, with a break in the slope occurring around 717 K. It is also coincident with changes in the unit cell along the *c* axis, suggesting thermal expansion of the new unit cell after the oxidation-driven shrinkage. Such slow oxidation event is again consistent with the TGA-DSC experiments, which showed a mass gain of 1.66% from 533 K to 923 K accompanying the broad exothermic DSC peak.

The CTEs (α_a and α_c) of Ce_{4.67}(SiO₄)₃O were determined for the first time by fitting the lattice expansion as a function of temperature. Along the *a* axis, two linear trends were established:

$$301\text{--}668 \text{ K} \quad a \text{ (\AA)} = 9.631 + 8.1 \times 10^{-5}T \quad R^2 = 0.986 \quad (3)$$

$$717\text{--}953 \text{ K} \quad a \text{ (\AA)} = 9.48 + 3.0 \times 10^{-4}T \quad R^2 = 0.989 \quad (4)$$

From these equations we derived CTE values of the *a*-axis to be $8.4 \times 10^{-6} \text{ K}^{-1}$ and $3.1 \times 10^{-5} \text{ K}^{-1}$, from 301 K to 668 K and from 717 K to 953 K, respectively. The α_a in high temperatures is thus 3.7 times higher than that before 668 K. Such an increase in the expansion rate can be attributed to the presence of additional oxygen in the coordinates of (0, 0, ¼) and (0, 0, ¾). The reason why the rate of expansion did not directly coincide with the additional “free oxygens” starting at 559 K and was delayed till after 717 K could be due to the competition caused by the contraction of the *c*-axis occurring over this temperature interval (Figure 5). In addition, the unit cell parameter *c* was fitted according to three linear relations:

$$301\text{--}513 \text{ K} \quad c \text{ (\AA)} = 7.080 + 4.3 \times 10^{-5}T \quad R^2 = 0.987 \quad (5)$$

$$559\text{--}668 \text{ K} \quad c \text{ (\AA)} = 7.195 - 16.7 \times 10^{-5}T \quad R^2 = 0.999 \quad (6)$$

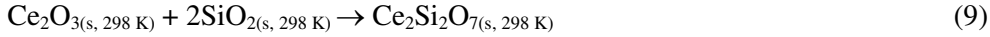
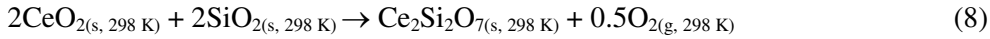
$$717\text{--}953 \text{ K} \quad c \text{ (\AA)} = 7.035 + 6.5 \times 10^{-5}T \quad R^2 = 0.920 \quad (7)$$

from which α_c values were derived as $6.0 \times 10^{-6} \text{ K}^{-1}$, $-23.5 \times 10^{-6} \text{ K}^{-1}$, and $9.2 \times 10^{-6} \text{ K}^{-1}$, for 301–513 K, 559–668 K, and 717–953 K, respectively. The ratio of axial CTEs α_a/α_c varies from 1.4 to 3.4, suggesting an anisotropic behavior of Ce_{4.67}(SiO₄)₃O and of Ce³⁺_{1.67-x}Ce⁴⁺_xCe³⁺₃(SiO₄)₃O_{1+0.5x}.

3.4. High temperature oxide melt drop solution calorimetry

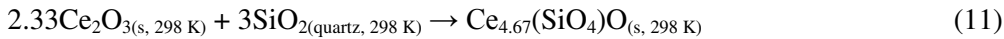
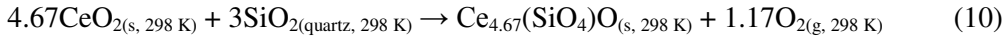
The enthalpy of formation (ΔH_f) and enthalpy of formation from oxides ($\Delta H_{f, \text{ox}}$) were determined for A-Ce₂Si₂O₇ and Ce_{4.67}(SiO₄)₃O by conducting high temperature oxide melt drop solution calorimetry in PbO·B₂O₃ solvent. Previously, the PbO·B₂O₃ solvent has been commonly used to dissolve silicate minerals,⁶⁰ including several different compositional types of rare-earth oxyapatites.^{23,69,70} We also tested the solvent on CeSiO₄ for dissolution prior to its use for the two Ce silicates. The resulted enthalpy of drop solutions (ΔH_{ds}) of CeSiO₄ was found to 133.64 kJ/mol, from which we derived $\Delta H_{f, \text{ox}} = 28.7 \text{ kJ/mol}$ and $\Delta H_f = -1970.7 \text{ kJ/mol}$ using the thermochemical cycle reported in Table S1. Both values are in excellent agreement with the previously enthalpies determined for CeSiO₄ using 3Na₂O·4MoO₃ solvent ($\Delta H_{f, \text{ox}} = 27.5 \pm 3.1 \text{ kJ/mol}$ and $\Delta H_f = -1971.9 \pm 3.6 \text{ kJ/mol}$).³³ Henceforth, we confirmed the complete dissolution of cerium silicate materials in PbO·B₂O₃ solvent.

The values of ΔH_{ds} were measured to be 140.05 ± 3.98 kJ/mol and 244.92 ± 6.66 kJ/mol for $\text{A-Ce}_2\text{Si}_2\text{O}_7$ and $\text{Ce}_{4.67}(\text{SiO}_4)_3\text{O}$, respectively. In order to derive their enthalpies of formation, we constructed two independent thermochemical cycles (shown in Tables 4 and 5) for each phase in order to check the data integrity and accuracy. The first one involved CeO_2 as the reference oxide while the second used Ce_2O_3 . The corresponding reactions of formation of $\text{A-Ce}_2\text{Si}_2\text{O}_7$ from these two different binary oxides were:



Using the thermochemical cycle reported in Table 4, the enthalpies of reactions (equations 8 and 9) were derived to be $\Delta H_{\text{f, ox}} = 173.7 \pm 5.5$ kJ/mol and -197.9 ± 7.4 kJ/mol, respectively. Consequently, the ΔH_{f} values associated with $\text{A-Ce}_2\text{Si}_2\text{O}_7$ was determined to be -3825.1 ± 6.0 kJ/mol and -3825.1 ± 9.5 kJ/mol. The two derived ΔH_{f} values were found to be identical within the experimental error, confirming the high data quality. Previously, ΔH_{f} of monoclinic $\text{G-Ce}_2\text{Si}_2\text{O}_7$ was determined by acid calorimetry to be -3807.6 ± 4.5 kJ/mol⁶⁷. So the enthalpy of transition for $\text{A-Ce}_2\text{Si}_2\text{O}_7 \rightarrow \text{G-Ce}_2\text{Si}_2\text{O}_7$ is 17.5 ± 7.5 kJ/mol, which is endothermic and needs energy to trigger such “sluggish” reconstructive transition¹⁶ from the low-temperature tetragonal A-phase to the high-temperature monoclinic G-phase.

We applied the same aforementioned calorimetric method to the following two reactions forming $\text{Ce}_{4.67}(\text{SiO}_4)_3\text{O}$:



By this way, we obtained $\Delta H_{\text{f, ox}}$ to be 421.4 ± 8.7 kJ/mol and -445.6 ± 11.6 kJ/mol (Table 5), from CeO_2 (equation 10), and from Ce_2O_3 (equation 11), respectively. Such a large differences between the two $\Delta H_{\text{f, ox}}$ values is that CeO_2 is more stable than Ce_2O_3 under standard condition at RT. The ΔH_{f} for $\text{Ce}_{4.67}(\text{SiO}_4)_3\text{O}$ was then determined to be -7391.3 ± 9.5 kJ/mol or -7391.3 ± 14.7 kJ/mol. Furthermore, by combining the above result with enthalpies of formation of other isostructural rare-earth oxyapatites (Sm , Nd , Gd)²³, we established a linear relation of $\Delta H_{\text{f, ox}}$ against ionic potential (Figure 10): $\Delta H_{\text{f, ox}}$ (kJ/mol) = $(-3374.4 \pm 102.6) + (1106.3 \pm 38.2) \cdot (Z/r)$, with an adjusted $R^2 = 0.996$. However, $\text{La}_{4.67}(\text{SiO}_4)_3\text{O}$ was found to be an outlier, as it significantly deviates from such trend. Risbud *et al.* argued that it could be due to the nonlinear effect of the ionic potential contributing to enthalpy, particularly as a flattening energetic surface from Nd to La .²³ However, with the newly available enthalpy of formation of $\text{Ce}_{4.67}(\text{SiO}_4)_3\text{O}$, we extended the linearity to beyond Nd , which ionic radius range includes some important actinides, such as Am and Pu .

4. Discussion

4.1. Aeronautic applications of A-Ce₂Si₂O₇ or Ce_{4.67}(SiO₄)₃O

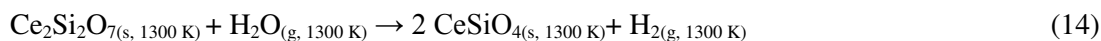
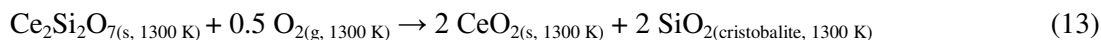
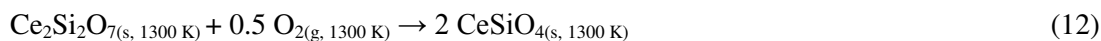
As it was stated earlier, one of the main expressed interest into rare earth silicate materials is their potentials as TBC or EBC against high temperature degradation commonly encountered in the aeronautical applications.^{1,2,10-13} Desirable TBC and EBC materials must have both structural and chemical stabilities.^{2,4,10-12,71-73} The structural stability includes congruent CTEs as the material that they are coating and phase stability at the operating temperature, which can minimize potential strains that promote mechanical failure.^{1,2,4-9,73-75} The chemical inertness allows for inhibition of corrosion to the given material that they are coating. As many next generation high-temperature alloys and CMC for aeronautical application offer superior thermal and mechanical properties at elevated temperature,^{71,76} they often rapidly degrade in the presence of high-temperature air, steam, or mineral debris.^{10-12,71} For this reason, the EBC or TBC must be chemically stable and resist corrosion, to sustain the operating lifespan. Hence, to fully assess the suitability of the materials for aeronautical applications, we evaluated the high temperature stability of both A-Ce₂Si₂O₇ and Ce_{4.67}(SiO₄)₃O in terms of both structural and chemical stability.

To assess the high temperature structural stability of A-Ce₂Si₂O₇, we calculated the Apparent Bulk Coefficients of Thermal Expansion (ABCTE)^{1,7} so that a direct comparison to the data reported by Fernández-Carrión *et al.*¹ and Ayyasamy *et al.*²² could be made. Here $(\Delta V/V_0)/3$ was plotted against ΔT (Figure 11), where $\Delta V = V - V_0$ (V is the measured volume at each temperature and V_0 is the volume obtained at T_0) and ΔT is the temperature interval of collecting the HT-XRD data ($\Delta T = T - T_0$ and $T_0 = 301$ K). A linear relation was found, $(\Delta V/V_0)/3 = (-1.9604 \pm 0.5800) \times 10^{-4} + (1.2425 \pm 0.0130) \times 10^{-5} \cdot \Delta T$ (adjusted $R^2 = 0.998$), from which the ABCTE of A-Ce₂Si₂O₇ was evaluated to be $12.42 \times 10^{-6} \text{ K}^{-1}$ (Table 6).

By combining the ABCTE value we obtained in this paper for A-Ce₂Si₂O₇, with the already reported ABCTEs of other A-Ln₂Si₂O₇ (Ln = La, Nd, Pr),¹ one may generate a general trend for predicting the ABCTEs of unknown disilicate compounds within the $P4_1$ space group. As it has been previously recognized that isostructural inorganic materials show an empirical correlation between thermodynamic variables, such as enthalpy,^{64,77-81} free energy,^{82,83} entropy,⁸⁴ or bulk modulus,^{85,86} to an underlying structural components, such as the cationic radii of a cation or the unit cell volume. So in this work, we used a linear regression to determine the contributions of ionic radii to ABCTEs (Table 6),¹ with the predicted trend exhibited in Figure 12. Additionally, the ABCTE of A-Ce₂Si₂O₇ derived by machine learning reported in Ayyasamy *et al.*²² agrees reasonably well (6% difference) with our value ($12.42 \times 10^{-6} \text{ K}^{-1}$) within the standard deviation of their predicted value. Such smaller calculated ABCTE could be due to the underestimation of the unit cell volume of A-Ce₂Si₂O₇ (Table 7).²² With such a high CTE, there could be applications for A-Ce₂Si₂O₇ for utilization as TBC of a metal substrate.¹ However, when considering high temperature structural stability, the A-Ce₂Si₂O₇ \rightarrow G-Ce₂Si₂O₇ transition at 1547 K could be considered as a drawback. As the temperature of the rear outlet in next generation combustion engines will

need to exceed 2123 K², such a transition is probable to occur. This will cause a large reduction in the unit cell volume ($\sim 46\%$)¹⁴ and a decrease in the CTE by roughly half (Table 1).¹ Such a reduction in both unit cell volume and CTE may cause for mechanical strain on the system, resulting in cracks and fissures to develop.

The assessment of the chemical stability of A-Ce₂Si₂O₇ was based on four reactions occurring in the presence of oxygen or water at 1300 K:



The temperature of 1300 K was chosen because it is below the A-Ce₂Si₂O₇ → G-Ce₂Si₂O₇ transition. As the thermodynamic stability of any given reaction is dictated by the Gibbs free energy $\Delta G = \Delta H - T\Delta S$, which requires both enthalpy and entropy. To date there has been no experimentally reported $S^\circ(298 \text{ K})$ value of either A-Ce₂Si₂O₇ or CeSiO₄. However, the S° value can be estimated through an empirical relation between the formula unit volume ($V_m = V_{\text{cell}} / \text{formula units (Z)}$)⁸⁷ and the standard entropies for silicate minerals.⁸⁴ We verified the accuracy of such method by calculating $S^\circ(298 \text{ K})$ of zircon, with the difference between the benchmarked ($84.0 \pm 1.3 \text{ J}/(\text{mol}\cdot\text{K})$)⁸⁸ and the estimated ($85.1 \pm 2.6 \text{ J}/(\text{mol}\cdot\text{K})$) being only 1.3%. The molar volumes V_m of A-Ce₂Si₂O₇ and of CeSiO₄ are $1143.40(2) \text{ \AA}^3/8$ (Table 2) and $298.93(1) \text{ \AA}^3/4$ ⁸⁹, respectively. The corresponding $S^\circ(298 \text{ K})$ were estimated to be $186.2 \pm 5.6 \text{ J}/(\text{mol}\cdot\text{K})$ and $97.9 \pm 2.9 \text{ J}/(\text{mol}\cdot\text{K})$, respectively. By combining with $S^\circ(298 \text{ K})$ of the constituent elements,⁸⁸ ΔS_f° was calculated and subsequently applied to evaluate ΔG_f° and ΔG_{rxn} (Table S2). The above methodology has been used successfully in estimating ΔG_f° of polyhalite (K₂Ca₂Mg(SO₄)₄·2H₂O) to determine its stability in a mined geological repository.⁹⁰ In order to obtain $\Delta H_f(1300\text{K})$, we used the thermodynamic function:

$$\Delta H(T) = \Delta H(298\text{K}) + \int_{298\text{K}}^T \Delta C_p dT. \quad (16)$$

When the C_p data of a given phase was not available, the Neumann-Kopp's rule was used. Neumann-Kopp's rule states that C_p of a complex oxide can be calculated through the summation of known C_p of its constituent binary oxides.⁹¹ We also verified such approximation by comparing the estimated C_p value with those reported for ZrSiO₄⁸⁸ and G-Ce₂Si₂O₇.⁹² For zircon, the difference between the two C_p values differed by a maximum of 1.1% over the temperature range of 500–1400 K. This was deemed acceptable to use for obtaining a C_p value for CeSiO₄. Conversely, for G-Ce₂Si₂O₇, it was found that the estimation underestimated the benchmarked C_p value by 6.1% at 1000 K (Figure S3). For this reason, we have chosen to use the experimentally derived C_p value of G-Ce₂Si₂O₇⁹² for A-Ce₂Si₂O₇ instead of using the C_p obtained through the Neumann-Kopp estimation. Here, we extended the benchmarked C_p equation of G-Ce₂Si₂O₇ from 900 K⁹² to 1300 K using a fifth order polynomial fit (Figure S3). The equation describing the new C_p

data is $y = (-29.42 \pm 1.141) + (1.518 \pm 0.025) \cdot x + (-0.004 \pm 0.025) \cdot x^2 + (4.533 \pm 0.432) \times 10^{-6} \cdot x^3 + (-2.881 \pm 0.491) \times 10^{-9} \cdot x^4 + (7.260 \pm 1.993) \times 10^{-13} \cdot x^5$, with an adjusted R^2 of 0.999 (Table S2).

When evaluating the calculated ΔG_{rxn} of reactions (Table S2), it is clear that A-Ce₂Si₂O₇ is chemically unstable in the presence of oxygen or steam at 1300 K and should undergo exothermic decomposition reactions into CeO₂ and SiO₂. This was demonstrated through $\Delta G_{rxn}(13) = -182.7 \pm 10.7$ kJ/mol and $\Delta G_{rxn}(14) = -223.3 \pm 10.7$ kJ/mol. The high temperature decomposition of A-Ce₂Si₂O₇ into CeSiO₄ in the presence of air at 1300 K (reaction (12)) was found to be favorable because of negative value of $\Delta H_{rxn}(1300K)$, -188.1 kJ/mol. This reaction was found to be -39.4 kJ/mol more favorable to occur than the degradation of A-Ce₂Si₂O₇ into CeO₂ and SiO₂ ($\Delta H_{rxn}(1300K) = -148.7$ kJ/mol). Nevertheless, due to the increased importance of ΔS term in assessing the thermodynamic stability (ΔG) at elevated temperatures, the reaction was ultimately found to be thermodynamically unfavorable, with $\Delta G_{rxn}(12) = 66.7 \pm 13.2$ kJ/mol at 1300 K (Table S2).

An overall evaluation of the suitability of Ce_{4.67}(SiO₄)₃O for high-temperature aeronautical applications can be made by analyzing the results of *in situ* HT-XRD (Figure 5) and TGA-DSC (Figure 9), both of which showed a thermal decomposition into a mixture of its binary oxides in the presences of O₂ at elevated temperatures. Therefore, from both a structural and chemical stability standpoint, Ce_{4.67}(SiO₄)₃O is not a good EBC or TBC material for high-temperature applications. However, it is known that various rare-earth oxyapatites (M²⁺RE₄(SiO₄)₃O) form as corrosion products between the rare-earth disilicates EBC and molten aerosol CMAS mineral dust,^{10,11,93} which implies that the cation-vacancy rare-earth oxyapatite (RE_{4.67}(SiO₄)₃O) may also form under such conditions. More generally, RE_{4.67}(SiO₄)₃O exhibit less negative enthalpy of formation values compared to Ca²⁺RE₄(SiO₄)₃O determined by Costa *et al.*¹¹. However, the higher disordering in the cation-vacancy phase have greater entropic contribution at high temperatures which could lead to its formation in the presence of molten CMAS. Although at temperature above ~1000 K, Ce_{4.67}(SiO₄)₃O is not thermally stable in the presence of O₂ and will decompose into CeO₂ and SiO₂.

4.2. Understanding of the mineral formation of stetindite and percleveite:

With the enthalpies of formation available now for the two naturally occurring cerium silicate phases of stetindite (CeSiO₄) and percleveite (A-Ce₂Si₂O₇), we can evaluate their formation under relevant geological settings, aiming to shed new light of the overall rarity. $\Delta H_{f,ox}$ of stetindite was reported to be 27.5 ± 3.1 kJ/mol.³³ This moderately endothermic $\Delta H_{f,ox}$ explains the difficulty in synthesizing CeSiO₄ in the laboratory and its rarity in nature because it is metastable with respect to its two binary oxides (CeO₂ and SiO₂), as it is found for coffinite.^{33,61,94-96} $\Delta H_{f,ox}$ of percleveite from CeO₂ and SiO₂ is 173.7 ± 5.5 kJ/mol, which also indicates that the formation of percleveite is not favorable.

Despite being thermodynamically unstable, both stetindite and percleveite have been found in mineral deposits. The geologic setting where these two minerals have been identified does differ from one

another. Stetindite was discovered at the Stetind pegmatite of the Tysfjord granite located in Norway.³⁶ Percleveite was discovered in an old museum specimen originating from the Bastnäs hydrothermal deposit located in Sweden and has since only been found within this specimen.³⁴ A possible explanation is that the mineral formation is largely dictated by the local redox conditions in the deposit. Mineral redox buffer assemblages are often used in the geochemical system to fix the oxygen fugacity (f_{O_2}).⁹⁷ Common mineral redox buffer assemblages include quartz-fayalite-magnetite (QFM), nickel-nickel oxide (Ni/NiO), and hematite-magnetite (Fe_2O_3/Fe_3O_4).⁹⁷ Particularly, hematite was found to be associated with the mineral deposit where stetindite was discovered,³⁶ creating a localized oxidizing environment, allowing for Ce^{4+} to form through the oxidation of Ce^{3+} -fluoride complex or other Ce^{3+} silicates such as percleveite.^{36,98} This does bear a similarity to the procedure described by Estevenon *et al.* for the hydrothermal synthesis of $CeSiO_4$ from both aqueous and solid precursors.^{37,99} Furthermore, the enthalpy of reaction of $A-Ce_2Si_2O_7 \rightarrow CeSiO_4$ at room temperature was evaluated to be -59.4 ± 4.1 kJ/mol per mole of Ce (and -63.8 ± 3.6 kJ/mol per mole of Ce for $Ce_{4.67}(SiO_4)_3O \rightarrow CeSiO_4$), and the Gibbs free energy of reaction under 523 K (the synthesis temperature for $CeSiO_4$)³⁷ to be -22.6 ± 7.9 per mole of Ce (and -5.7 ± 7.2 kJ/mol per mole of Ce for $Ce_{4.67}(SiO_4)_3O \rightarrow CeSiO_4$), suggesting a favorable proceeding of forming tetravalent cerium orthosilicate from trivalent cerium silicates. Thus, under geologic conditions, Ce^{3+} silicates could serve as potential solid precursors if the local redox of the deposit conditions became oxidizing, such as what was observed at the deposit where stetindite was discovered.^{36,98} For percleveite, magnetite is associated with the mineral deposit,³⁴ acting as the redox buffer controlling the formation of percleveite. It is further supported by the thermodynamically favorable enthalpy of formation of percleveite from Ce_2O_3 and SiO_2 , -197.9 ± 7.4 kJ/mol. This is also consistent with the synthetic procedure of $A-Ce_2Si_2O_7$ where a high temperature reducing condition (H_2 atmosphere) was used to suppress the oxidative formation of CeO_2 .^{14,16,21,27,37}

While the above offers both a formational mechanism for $CeSiO_4$ in nature and its overall rarity, it does not offer a direct explanation to why $A-Ce_2Si_2O_7$ is so rare in nature. As the mineral assemblages to form a reducing environment are possible to occur across the entire spectrum of the igneous classification, from mafic to felsic,^{44,97} and as Ce concentrations are also relatively conserved across the igneous classification,^{100,101} one would expect percleveite to be observed at more than just one mineral deposit.^{34,102} Interestingly, at the one mineral deposit (Bastnas, Sweden) where percleveite was discovered, the mineral was found to be a primary mineral along with that of cerite $(Ce,Ca)_9(Fe^{3+},Mg)(SiO_4)_6(SiO_3OH)(OH)_3$,³⁴ with each of these forming before that of the more widely abundant minerals of allanite $((Ca,Ce)_2(AlFe^{3+})_3(Si_2O_7)(SiO_4)O(OH))$ and bastnäsite $(REECO_3F)$.¹⁰³ This could indicate that percleveite serves as the precursor to allanite and bastnäsite not only at the Bastnas deposit, but also at other hydrothermal rare earth deposits where both allanite and bastnäsite are commonly observed. This is further supported by the observation of bastnäsite-(Ce) being found growing at the expense of the percleveite

holotype.¹⁰² Such a hypothesis is similar to the proposed explanation for the rarity of fluocerite (REEF₃), as it is converted to bastnäsite in carbonate rich fluids.^{102,104,105}

4.3. Relevance in the field of the nuclear fuel cycle:

Although Ce_{4,67}(SiO₄)₃O and other cation vacant rare earth oxyapatite have not been discovered as natural phases, they do find significant relevance to both the middle and end of the “cradle to grave” aspect of the nuclear fuels cycle. For example, when simulating the vitrification process for immobilizing nuclear waste in alumino-borosilicate glasses it was found that Dy and Ho cation-vacant oxyapatites formed within the simulated nuclear waste glass.¹⁰⁶ Further, in a study using cerium silicide (a surrogate for uranium silicide fuel) to evaluate the performance under the hydrothermal conditions (573 K and 9MPa) presented in a light water reactor (LWR), Ce_{4,67}(SiO₄)₃O was always found as a corrosion layer to cerium silicide.¹⁰⁷ Therefore, it is clear that An_{4,67}(SiO₄)₃O type-materials could be also potentially formed during the long-term storage under geological repository resulting in the breach of the radiological waste canister. Assuming the former scenario, the enthalpies of formation of Am_{4,67}(SiO₄)₃O and Pu_{4,67}(SiO₄)₃O from oxides were predicted to be -340.4 kJ/mol and -384.9 kJ/mol, respectively, based on the linear relation given in Figure 10. Similar methodology was utilized for predicting $\Delta H_{f, ox}$ for actinide orthosilicates.³³

In the mined geological repository, the local redox environment would be fixed to be reducing.^{108–}
¹¹⁰ Achieving such reducing environments can be done through controlling the fugacity of oxygen and other gasses through various mineral assemblages, such as was described in the previous section.⁹⁷ Such engineering was demonstrated at the Waste Isolation Pilot Plant (WIPP) in New Mexico, USA, where periclase (MgO) was used to hinder microbial breakdown of organics and scavenge for CO₂.¹¹¹ The presence of remaining organics could further lead to reducing conditions in the repository. Thus, it is reasonable to assume that in the unlikely event of canister failure, the waste package will interact with infiltrated ground water under reducing environment. Under such conditions, Pu could be found in the trivalent state and readily involved in the formation of Pu_{4,67}(SiO₄)₃O. For Am, these findings are slightly more significant due to its predominant trivalent oxidation state.^{112–115} Therefore, if any Am³⁺ would react with silica, it would be thermodynamically favorable to form Am_{4,67}(SiO₄)₃O. However, if the redox environment becomes oxidative, transformation from trivalent actinide silicates to the tetravalent actinide orthosilicate may occur driven by thermodynamics, such as that demonstrated in the case of A-Ce₂Si₂O₇ → CeSiO₄ or Ce_{4,67}(SiO₄)₃O → CeSiO₄. Lastly, as actinides are known to form nanoparticles in reactive silicate rich fluids^{45–48}, it could enable the actinide silicate complexes or compounds to be transported in colloidal forms immense distances away from a breached canister if the particles would not settle.^{53,54}

5. Conclusions

Through thermogravimetric analysis coupled differential scanning calorimetry (TGA-DSC), *in situ* high temperature synchrotron XRD, and high temperature oxide melt drop solution calorimetry, the thermodynamic parameters of percleveite ($\text{A-Ce}_2\text{Si}_2\text{O}_7$) and cerium oxyapatite ($\text{Ce}_{4.67}(\text{SiO}_4)_3\text{O}$) were determined. The results of the TGA-DSC confirmed that percleveite and cerium oxyapatite were thermally stable under nitrogen. However, both the TGA-DSC and *in situ* synchrotron HT-XRD showed that cerium oxyapatite was not thermally stable under an oxygen atmosphere undergoing a slow partial oxidation of Ce^{3+} to new nonstoichiometric phases $\text{Ce}^{3+}_{1.67-x}\text{Ce}^{4+}_x\text{Ce}^{3+}_3(\text{SiO}_4)_3\text{O}_{1+0.5x}$, which then decomposed to CeO_2 and SiO_2 above ~ 1000 K. *In situ* synchrotron HT-XRD revealed that the ABCTE of percleveite is $12.4 \times 10^{-6} \text{ K}^{-1}$, which follows the systematic linear trend exhibited by the other A- $\text{RE}_2\text{Si}_2\text{O}_7$ ($P4_1$). Through high temperature oxide melt drop solution calorimetry, the ΔH_f was determined to be -3825.1 ± 6.0 kJ/mol for percleveite and -7391.3 ± 9.5 kJ/mol for cerium oxyapatite. We further evaluated the roles of A- $\text{Ce}_2\text{Si}_2\text{O}_7$ and $\text{Ce}_{4.67}(\text{SiO}_4)_3\text{O}$ as TBC/EBC or potential degradation products in the field of high-temperature applications, and as possible alteration phases and surrogate materials in the geological nuclear waste repository. Lastly, the geological relevance of percleveite was discussed and its overall role as a possible precursor for allanite-(Ce) and stetindite.

Acknowledgements

This work was supported by the institutional funds from the Department of Chemistry at Washington State University. We also acknowledge the support by the U.S. Department of Energy, Office of Nuclear Energy, grants DE-NE0008582 and DE-NE0008689. This research used Beamline 28-ID-2 (XPD) of the National Synchrotron Light Source II, a U.S. Department of Energy (DOE) Office of Science User Facility operated for the DOE Office of Science by Brookhaven National Laboratory under Contract No. DE-SC0012704. Portions of this research were also supported by collaboration, services, and infrastructure through the Nuclear Science Center User Facility at WSU, the WSU-PNNL Nuclear Science and Technology Institute, and Alexandra Navrotsky Institute for Experimental Thermodynamics. We are grateful for the discussions and comments with A.A. Migdisov, in especially for his guidance in understanding mineral redox buffers. Lastly, we thank A. Navrotsky for supplying us Pt crucibles and lead borate solvent for the calorimetric experiments in this work.

Author contributions

X.G. conceived the research. A.C.S. & K.W.K. performed DSC and high temperature drop solution oxide melt calorimetry. P.E. synthesized all phases. X.G., V.G.G., and J.B. performed ambient and high temperature synchrotron XRD. A.C.S and X.G. analyzed and refined all the ambient and high temperature synchrotron XRD. All authors participated in discussions, interpretation of the data and writing of the manuscripts.

Tables

Table 1. Summary of CTE values for CMC and TBC/EBC materials.

Category	Material	CTE (10^{-6} K^{-1})	Reference
CMC	Si	4.0	4
CMC	SiC	5.0	4
CMC	Si ₃ N ₄	3.5	4
CMC	MoSi ₂	8.5	5
TBC/EBC	Mullite	5.4	4,6
TBC/EBC	δ -RE ₂ Si ₂ O ₇	7.7	1,7
TBC/EBC	γ -RE ₂ Si ₂ O ₇	4.1	1,7-9
TBC/EBC	β -RE ₂ Si ₂ O ₇	4.4	1,7,76
TBC/EBC	α -RE ₂ Si ₂ O ₇	8.3	1,7
TBC/EBC	G-RE ₂ Si ₂ O ₇	6.6	1
TBC/EBC	A-RE ₂ Si ₂ O ₇	12.1	1
Substrate of TBC	IN737 Superalloy	16.0	6

Table 2. Summary of unit cell parameters and refinement agreements for A-Ce₂Si₂O₇.

Temperature (K)	<i>a</i> (Å)	<i>c</i> (Å)	Volume (Å ³)	<i>R</i> _{wp} (%)
301	6.79901(7)	24.7346(2)	1143.40(2)	2.18
357	6.80225(7)	24.7469(2)	1145.05(2)	2.21
411	6.80677(9)	24.7633(2)	1147.34(3)	2.65
460	6.8104(1)	24.7772(2)	1149.19(3)	2.91
512	6.8147(1)	24.7929(2)	1151.40(3)	3.00
553	6.8187(1)	24.8065(3)	1153.38(4)	3.14
611	6.8231(1)	24.8232(3)	1155.64(4)	3.29
671	6.8284(1)	24.8439(3)	1158.41(5)	3.88
704	6.8327(2)	24.8595(4)	1160.60(5)	4.05
787	6.8365(2)	24.8729(4)	1162.52(5)	4.27
816	6.8410(2)	24.8901(4)	1164.85(6)	4.75
868	6.8452(2)	24.9057(5)	1166.99(6)	4.95
911	6.8488(2)	24.9191(5)	1168.85(6)	4.94
956	6.8528(2)	24.9336(5)	1170.90(7)	5.06
1001	6.8565(2)	24.9471(5)	1172.78(7)	5.22
1052	6.8599(2)	24.9591(5)	1174.53(7)	5.38

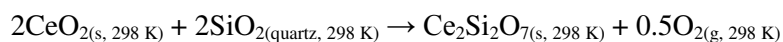
Table 3. Summary of unit cell parameters, refinement agreements, and values for x for ${}^{\text{XI}}\text{Ce}^{3+}_{1.67-}$
 ${}_x^{\text{IX}}\text{Ce}^{4+}_x {}^{\text{VII}}\text{Ce}^{3+}_3 (\text{IV}\text{Si}^{\text{IV}}\text{O}_4)_3 \text{III}\text{O}_{1+0.5x}$ ($0 < x < 0.27$).

Temperature (K)	a (Å)	c (Å)	Volume (Å ³)	R_{wp} (%)	x
301	9.6562(7)	7.0933(2)	572.78(5)	7.18	0.00
356	9.6604(7)	7.0956(2)	573.47(5)	7.07	0.00
408	9.6640(7)	7.0981(2)	574.10(5)	6.96	0.00
459	9.6664(6)	7.0994(2)	574.49(4)	6.80	0.00
513	9.6724(6)	7.1026(1)	575.46(4)	6.43	0.00
559	9.6776(6)	7.1023(1)	576.05(4)	5.92	0.04
617	9.6797(6)	7.0927(1)	575.53(4)	5.91	0.08
668	9.6864(6)	7.0841(2)	575.62(4)	6.05	0.11
717	9.6965(7)	7.0835(2)	576.78(5)	6.13	0.15
762	9.7089(8)	7.0871(2)	578.55(6)	6.45	0.18
818	9.720(1)	7.0879(2)	579.97(7)	6.84	0.23
863	9.739(1)	7.0928(3)	582.6(1)	7.28	0.26
907	9.749(2)	7.0936(4)	583.9(1)	7.84	0.27
954	9.767(3)	7.1004(6)	586.6(2)	8.58	0.27

Table 4. Thermochemical cycles used for calculations of the enthalpy of formation from binary oxides and the standard enthalpy of formation of percleveite based on the data of drop solution calorimetry in molten lead borate at 973 K.

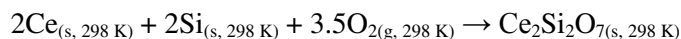
Reaction	ΔH (kJ/mol)
(1) $\text{Ce}_2\text{Si}_2\text{O}_7(\text{s}, 298 \text{ K}) + 0.5\text{O}_2(\text{g}, 973 \text{ K}) \rightarrow 2\text{CeO}_2(\text{sln}, 973 \text{ K}) + 2\text{SiO}_2(\text{sln}, 973 \text{ K})$	$\Delta H_1 = 140.05^* \pm 3.98^\ddagger (5)^\ddagger$
(2) $\text{CeO}_2(\text{s}, 298 \text{ K}) \rightarrow \text{CeO}_2(\text{sln}, 973 \text{ K})$	$\Delta H_2 = 122.9 \pm 2.6^{30}$
(3) $\text{SiO}_2(\text{quartz}, 298 \text{ K}) \rightarrow \text{SiO}_2(\text{sln}, 973 \text{ K})$	$\Delta H_3 = 39.4 \pm 0.4^{60}$
(4) $\text{O}_2(\text{g}, 298 \text{ K}) \rightarrow \text{O}_2(\text{g}, 973 \text{ K})$	$\Delta H_4 = 21.74 \pm 0.02^{88}$
(5) $\text{Ce}(\text{s}, 298 \text{ K}) + \text{O}_2(\text{g}, 298 \text{ K}) \rightarrow \text{CeO}_2(\text{s}, 298 \text{ K})$	$\Delta H_5 = -1088.7 \pm 1.5^{88}$
(6) $\text{Si}(\text{s}, 298 \text{ K}) + \text{O}_2(\text{g}, 298 \text{ K}) \rightarrow \text{SiO}_2(\text{quartz}, 298 \text{ K})$	$\Delta H_6 = -910.7 \pm 1.0^{88}$
(7) $2\text{CeO}_2(\text{s}, 298 \text{ K}) \rightarrow \text{Ce}_2\text{O}_3(\text{s}, 298 \text{ K}) + 0.5\text{O}_2(\text{g}, 298 \text{ K})$	$\Delta H_7 = 371.6 \pm 5.0$
(8) $2\text{Ce}(\text{s}, 298 \text{ K}) + 1.5\text{O}_2(\text{s}, 298 \text{ K}) \rightarrow \text{Ce}_2\text{O}_3(\text{s}, 298 \text{ K})$	$\Delta H_8 = -1805.8 \pm 5.8$

Enthalpy of formation from oxides of percleveite from CeO_2 :



$$\Delta H_{f, \text{ox}}(\text{Ce}_2\text{Si}_2\text{O}_7) = -\Delta H(1) + 2\Delta H_2 + 2\Delta H_3 - 0.5\Delta H_4 = 173.7 \pm 5.5 \text{ kJ/mol}$$

Standard enthalpy of formation of percleveite from CeO_2 :

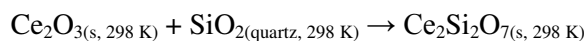


$$\Delta H_{f, \text{ox}}^{\text{p}}(\text{Ce}_2\text{Si}_2\text{O}_7) = \Delta H_{f, \text{ox}}(\text{Ce}_2\text{Si}_2\text{O}_7) + 2\Delta H_5 + 2\Delta H_6 = -3825.1 \pm 6.0 \text{ kJ/mol}$$

Standard enthalpy of formation of percleveite from CeO_2 normalized to 1 mol Ce:

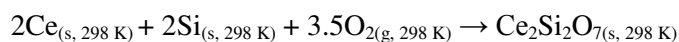
$$\Delta H_{f, \text{ox}}^{\text{p}}(\text{CeSiO}_{3.5}) = -1912.6 \pm 3.0 \text{ kJ/mol}$$

Enthalpy of formation from oxides of percleveite from Ce_2O_3 :



$$\Delta H_{f, \text{ox}}(\text{Ce}_2\text{Si}_2\text{O}_7) = -\Delta H_1 + 2\Delta H_2 + 2\Delta H_3 - 0.5\Delta H_4 - \Delta H_7 = -197.9 \pm 7.4 \text{ kJ/mol}$$

Standard enthalpy of formation of percleveite from Ce_2O_3 :



$$\Delta H_{f, \text{ox}}^{\text{p}}(\text{Ce}_2\text{Si}_2\text{O}_7) = \Delta H_{f, \text{ox}}(\text{Ce}_2\text{Si}_2\text{O}_7) + 2\Delta H_6 + \Delta H_8 = -3825.1 \pm 9.5 \text{ kJ/mol}$$

Standard enthalpy of formation of percleveite from Ce_2O_3 normalized to 1 mol Ce:

$$\Delta H_{f, \text{ox}}^{\text{p}}(\text{CeSiO}_{3.5}) = -1912.6 \pm 4.8 \text{ kJ/mol}$$

*Average. †Two standard deviations of the average value. ‡Number of measurements.

Table 5. Thermochemical cycles used for calculations of the enthalpy of formation from binary oxides and the standard enthalpy of formation of cerium oxyapatite based on the data of drop solution calorimetry in molten lead borate at 973 K.

Reaction	ΔH (kJ/mol)
(1) $\text{Ce}_{4.67}(\text{SiO}_4)_3\text{O}_{(s, 298 \text{ K})} + 1.17\text{O}_{2(g, 973 \text{ K})} \rightarrow 4.67\text{CeO}_{2(\text{sln}, 973 \text{ K})} + 3\text{SiO}_{2(\text{sln}, 973 \text{ K})}$	$\Delta H_1 = 244.92 \pm 6.66$ (4)
(2) $\text{CeO}_{2(s, 298 \text{ K})} \rightarrow \text{CeO}_{2(\text{sln}, 973 \text{ K})}$	$\Delta H_2 = 122.9 \pm 2.6^{30}$
(3) $\text{SiO}_{2(\text{quartz}, 298 \text{ K})} \rightarrow \text{SiO}_{2(\text{sln}, 973 \text{ K})}$	$\Delta H_3 = 39.4 \pm 0.4^{60}$
(4) $\text{O}_{2(g, 298 \text{ K})} \rightarrow \text{O}_{2(g, 973 \text{ K})}$	$\Delta H_4 = 21.74 \pm 0.02^{88}$
(5) $\text{Ce}_{(s, 298 \text{ K})} + \text{O}_{2(g, 298 \text{ K})} \rightarrow \text{CeO}_{2(s, 298 \text{ K})}$	$\Delta H_5 = -1088.7 \pm 1.5^{88}$
(6) $\text{Si}_{(s, 298 \text{ K})} + \text{O}_{2(g, 298 \text{ K})} \rightarrow \text{SiO}_{2(\text{quartz}, 298 \text{ K})}$	$\Delta H_6 = -910.7 \pm 1.0^{88}$
(7) $2\text{CeO}_{2(s, 298 \text{ K})} \rightarrow \text{Ce}_2\text{O}_{3(s, 298 \text{ K})} + 0.5\text{O}_{2(g, 298 \text{ K})}$	$\Delta H_7 = 371.6 \pm 5.0$
(8) $2\text{Ce}_{(s, 298 \text{ K})} + 1.5\text{O}_{2(s, 298 \text{ K})} \rightarrow \text{Ce}_2\text{O}_{3(s, 298 \text{ K})}$	$\Delta H_8 = -1805.8 \pm 5.8$
Enthalpy of formation from oxides of cerium oxyapatite from CeO_2:	
$4.67\text{CeO}_{2(s, 298 \text{ K})} + 3\text{SiO}_{2(\text{quartz}, 298 \text{ K})} \rightarrow \text{Ce}_{4.67}(\text{SiO}_4)\text{O}_{(s, 298 \text{ K})} + 1.17\text{O}_{2(g, 298 \text{ K})}$	
$\Delta H_{f, \text{ox}}(\text{Ce}_{4.67}(\text{SiO}_4)_3\text{O}) = -\Delta H_1 + 4.67\Delta H_2 + 3\Delta H_3 - 1.17 \Delta H_4 = 421.4 \pm 8.7 \text{ kJ/mol}$	
Standard enthalpy of formation of cerium oxyapatite from CeO_2:	
$4.67\text{Ce}_{(s, 298 \text{ K})} + 3\text{Si}_{(s, 298 \text{ K})} + 6.5\text{O}_{2(g, 298 \text{ K})} \rightarrow \text{Ce}_{4.67}(\text{SiO}_4)\text{O}_{(s, 298 \text{ K})}$	
$\Delta H_{f, \text{ox}}^\circ(\text{Ce}_{4.67}(\text{SiO}_4)_3\text{O}) = \Delta H_{f, \text{ox}}(\text{Ce}_{4.67}(\text{SiO}_4)_3\text{O}) + 4.67\Delta H_5 + 3\Delta H_6 = -7391.3 \pm 9.5 \text{ kJ/mol}$	
Standard enthalpy of formation of cerium oxyapatite from CeO_2 normalized to 1 mol Ce:	
$\Delta H_{f, \text{ox}}^\circ(\text{CeSi}_{0.64}\text{O}_{2.78}) = -1582.7 \pm 2.0 \text{ kJ/mol}$	
Enthalpy of formation from oxides of cerium oxyapatite from Ce_2O_3:	
$2.33\text{Ce}_2\text{O}_{3(s, 298 \text{ K})} + 3\text{SiO}_{2(\text{quartz}, 298 \text{ K})} \rightarrow \text{Ce}_{4.67}(\text{SiO}_4)\text{O}_{(s, 298 \text{ K})}$	
$\Delta H_{f, \text{ox}}(\text{Ce}_{4.67}(\text{SiO}_4)_3\text{O}) = -\Delta H_1 + 4.67\Delta H_2 + 3\Delta H_3 - 1.17\Delta H_4 - 2.33\Delta H_7 = -445.6 \pm 11.6 \text{ kJ/mol}$	
Standard enthalpy of formation of cerium oxyapatite from Ce_2O_3:	
$4.67\text{Ce}_{(s, 298 \text{ K})} + 2\text{Si}_{(s, 298 \text{ K})} + 6.5\text{O}_{2(g, 298 \text{ K})} \rightarrow \text{Ce}_{4.67}(\text{SiO}_4)\text{O}_{(s, 298 \text{ K})}$	
$\Delta H_{f, \text{ox}}^\circ(\text{Ce}_{4.67}(\text{SiO}_4)_3\text{O}) = \Delta H_{f, \text{ox}}(\text{Ce}_{4.67}(\text{SiO}_4)_3\text{O}) + 3\Delta H_6 + 4.67\Delta H_8 = -7391.3 \pm 14.7 \text{ kJ/mol}$	
Standard enthalpy of formation of cerium oxyapatite from Ce_2O_3 normalized to 1 mol Ce:	
$\Delta H_{f, \text{ox}}^\circ(\text{CeSi}_{0.64}\text{O}_{2.78}) = -1582.7 \pm 2.1 \text{ kJ/mol}$	

Table 6. Apparent Bulk Coefficients of Thermal Expansion (ABCTE) values for A-RE₂Si₂O₇ compound and their average ionic radii of each of the RE³⁺. The A-RE₂Si₂O₇ unit cell belong to the *P4₁* space group which exhibits four different crystallographic sites for the RE³⁺. These four sites differ in coordination with having coordination numbers of 7, 8, 9, and 9. For this reason averaging was done through taking the reported ionic size⁶⁸ of the RE³⁺ cation in each of the four coordination environments.

Chemical Formula	Avg. Ionic Radii of		Reference
	A-Site (Å) ⁶⁸	ABCTE (10 ⁻⁶ K ⁻¹)	
A-Pr ₂ Si ₂ O ₇	1.137	11.8	Fernandez-Carrion <i>et al.</i> (2013) ¹
A-Nd ₂ Si ₂ O ₇	1.121	10.5	Fernandez-Carrion <i>et al.</i> (2013) ¹
A-La ₂ Si ₂ O ₇	1.173	14.0	Fernandez-Carrion <i>et al.</i> (2013) ¹
A-Ce ₂ Si ₂ O ₇ [*]	1.151	11.7	Ayyasamy <i>et al.</i> (2020) ²²
A-Ce ₂ Si ₂ O ₇	1.151	12.4	This Study

* Calculated value

Table 7. Reported unit cell parameters for A-Ce₂Si₂O₇

Chemical	<i>a</i> (Å)	<i>c</i> (Å)	Volume (Å ³)	Reference
A-Ce ₂ Si ₂ O ₇	6.7964(3)	24.7282(14)	1142.22(10)	Deng & Ibers (2005) ⁵⁸
A-Ce ₂ Si ₂ O ₇	6.7920	24.7000	1139.38	Tas & Akinc (1994) ²⁷
Percleveite-(Ce)	6.7805(8)	24.689(5)	1135.1(3)	Holtstam <i>et al.</i> (2003) ³⁴
A-Ce ₂ Si ₂ O ₇	6.75781	24.5511	1121.20	Ayyasamy <i>et al.</i> (2020) ²²
A-Ce ₂ Si ₂ O ₇	6.7965(3)	24.7258(14)	1142.1(1)	Estevenon <i>et al.</i> (2019) ³⁷
A-Ce ₂ Si ₂ O ₇	6.79901(7)	24.7346(2)	1143.40(2)	This Study

Figures

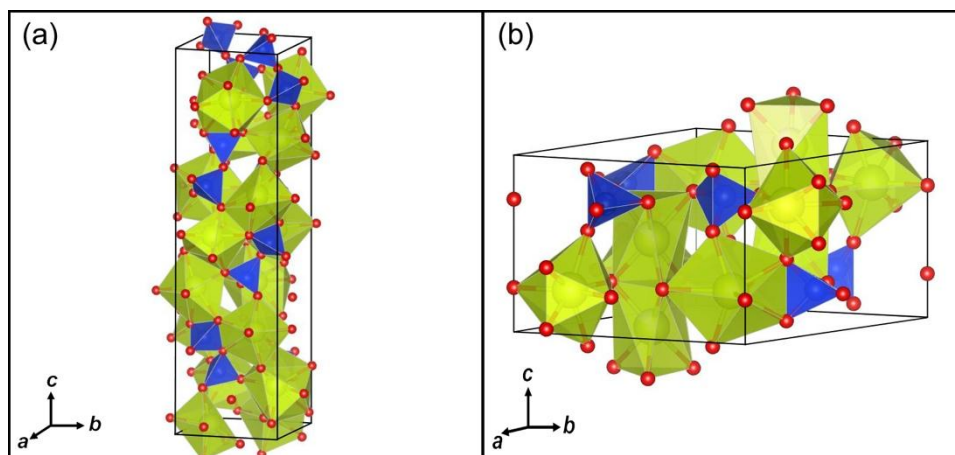


Figure 1. Structures of (a) $A\text{-Ce}_2\text{Si}_2\text{O}_7$ (space group: $P4_1$) and (b) $\text{Ce}_{4.67}(\text{SiO}_4)_3\text{O}$ (space group: $P6_3/m$).^{58,59,116}

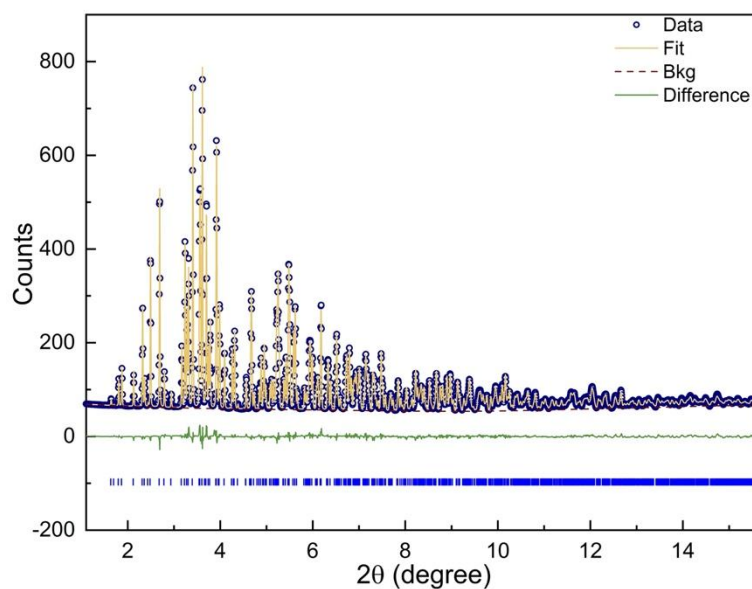


Figure 2. Fitted synchrotron XRD patterns of $A\text{-Ce}_2\text{Si}_2\text{O}_7$ collected at 301 K. Data are shown as *blue circles* signs and the *solid yellow curve* is the best fit obtained from the data. The *green dashed curve* represents the difference between the observed and calculated profiles. The *blue tick marks* above the *x-axis* indicates the positions of allowed diffraction maxima.

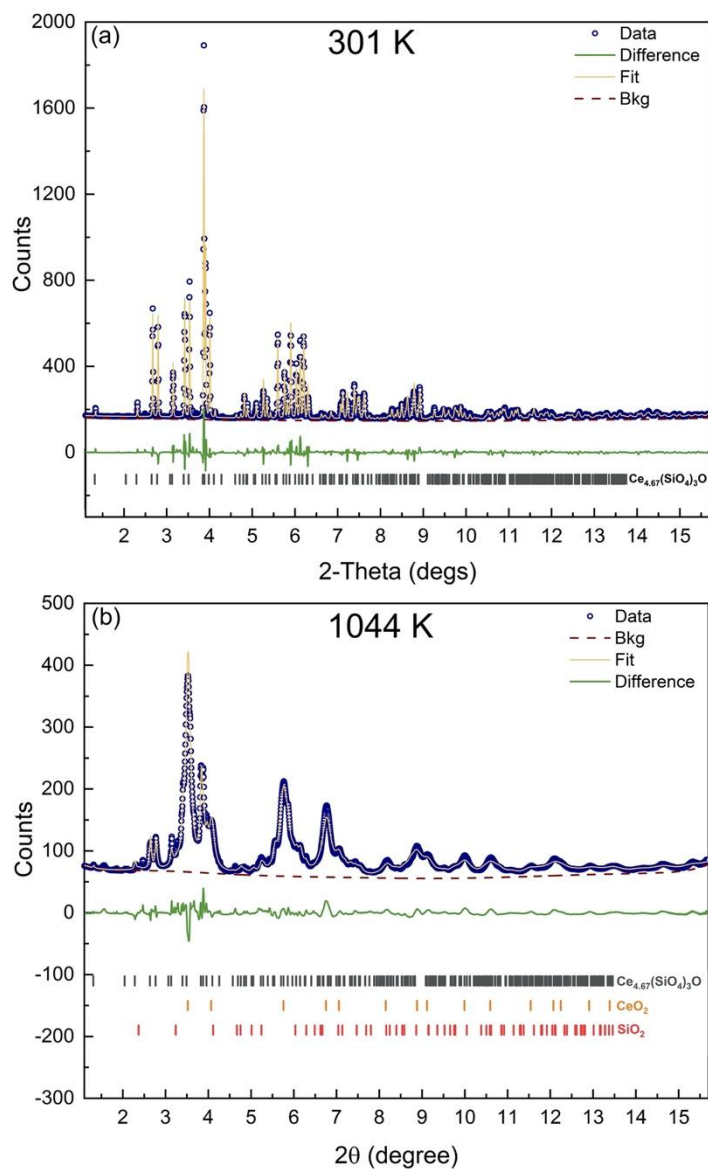


Figure 3. Fitted synchrotron XRD patterns of $\text{Ce}_{4.67}(\text{SiO}_4)_3\text{O}$ at (a) 301 K and (b) 1044 K. Data are shown as *blue circles* signs. The *solid yellow curve* is the best fit to the data. The *green dashed curve* represents the difference between the observed and calculated profiles. The *tick marks* above the *x-axis* indicate the positions of allowed diffraction maxima for $\text{Ce}_{4.67}(\text{SiO}_4)_3\text{O}$ (*gray*), CeO_2 (*orange*), and SiO_2 (*red*).

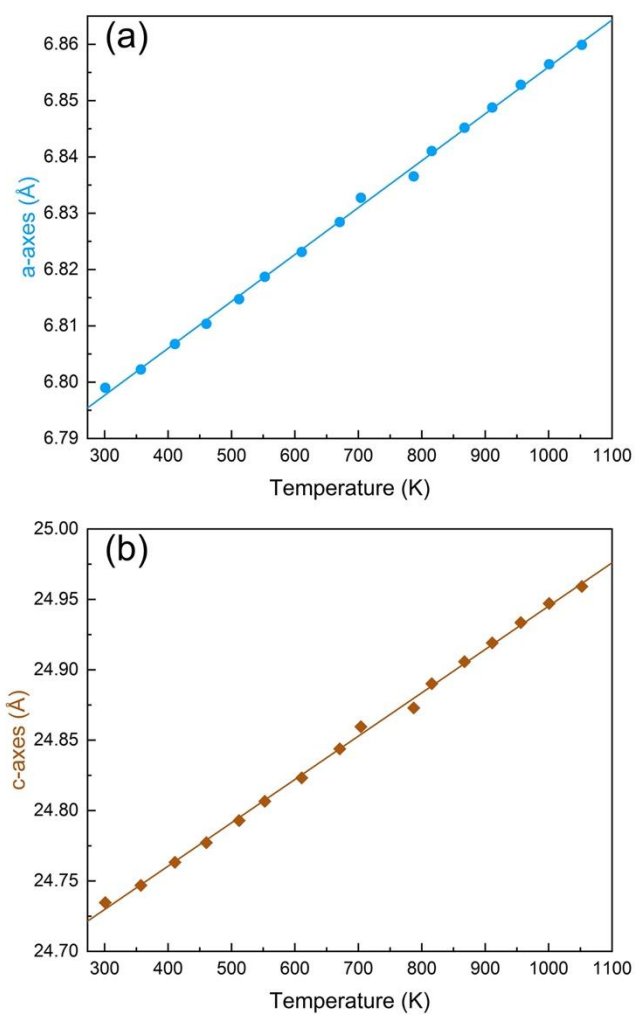


Figure 4. Variation of the unit cell parameters of A-Ce₂Si₂O₇ as a function of temperature. The equation of the line describing (a) is $a(\text{Å}) = (6.7726 \pm 0.0006) + (8.33 \pm 0.08) \times 10^{-5} \cdot x$ (with $R^2 = 0.998$); describing (b) is $c(\text{Å}) = (24.637 \pm 0.002) + (3.08 \pm 0.03) \times 10^{-4} \cdot x$ (with $R^2 = 0.998$).

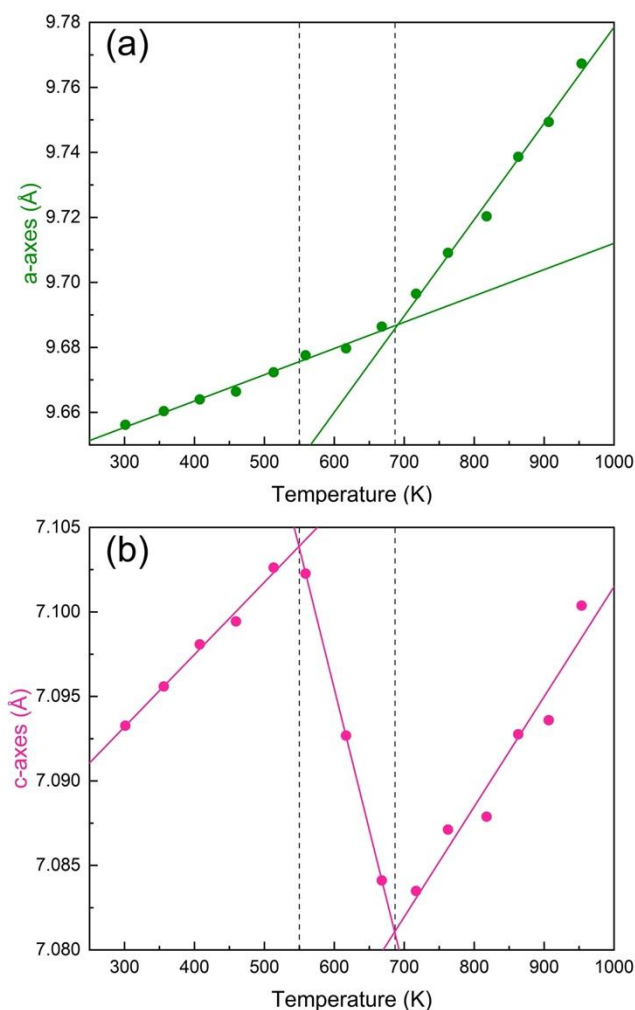


Figure 5. Unit cell parameters as a function of temperature for $\text{Ce}_{4.67}(\text{SiO}_4)_3\text{O}$. The equation of the line describing the variation of a is a (Å) = $(9.631 \pm 0.002) + (8.1 \pm 0.4) \times 10^{-5} \cdot x$ between 301K and 668K (with $R^2 = 0.986$), a (Å) = $(9.48 \pm 0.01) + (3.0 \pm 0.1) \times 10^{-5} \cdot x$ between 717K and 953K (with $R^2 = 0.989$); c (Å) = $(7.080 \pm 0.001) + (4.3 \pm 0.2) \times 10^{-5} \cdot x$ between 301K and 513K (with $R^2 = 0.987$), c (Å) = $(7.1954 \pm 0.0005) - (16.66 \pm 0.08) \times 10^{-5} \cdot x$ (with $R^2 = 0.999$) between 559K and 668K, and c (Å) = $(7.035 \pm 0.007) + (6.5 \pm 0.9) \times 10^{-5} \cdot x$ (with $R^2 = 0.920$) between 717K and 953K.

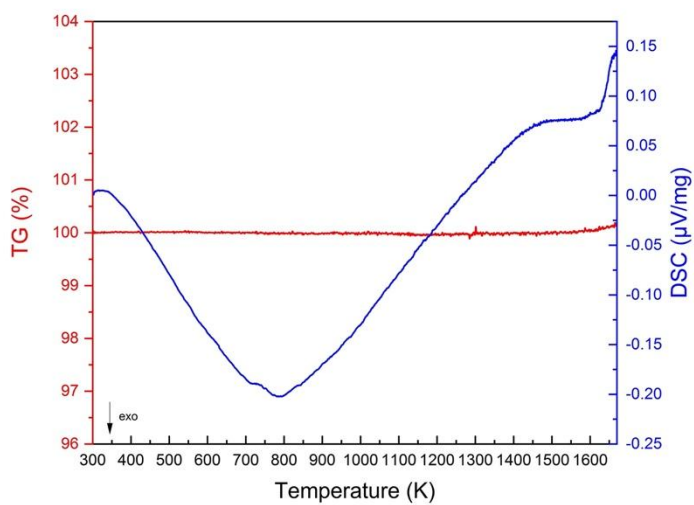


Figure 6. TGA-DSC of A-Ce₂Si₂O₇ under a N₂ atmosphere (starting sample mass of 7.655 mg).

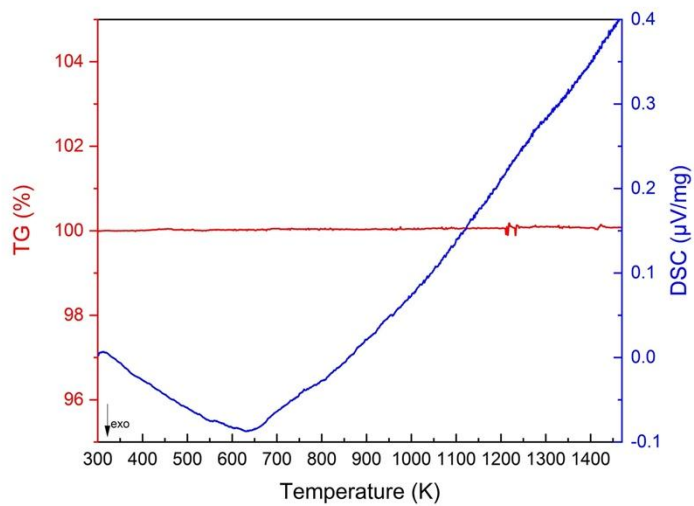


Figure 7. TGA-DSC of Ce_{4.67}(SiO₄)₃O under a N₂ atmosphere (starting sample mass of 4.885 mg).

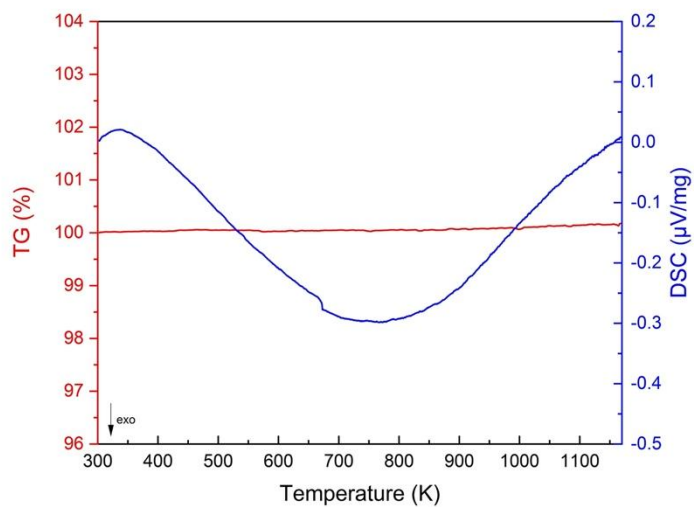


Figure 8. TGA-DSC of A-Ce₂Si₂O₇ under a synthetic air atmosphere (starting sample mass of 4.345 mg).

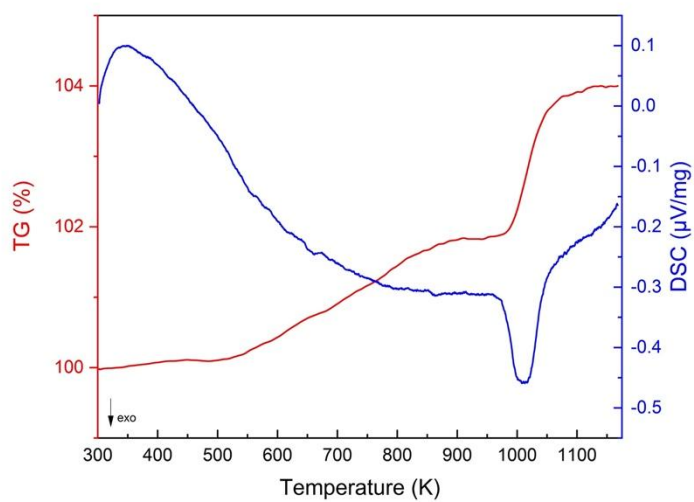


Figure 9. TGA-DSC of Ce_{4.67}(SiO₄)₃O under a synthetic air atmosphere (starting sample mass of 1.901 mg).

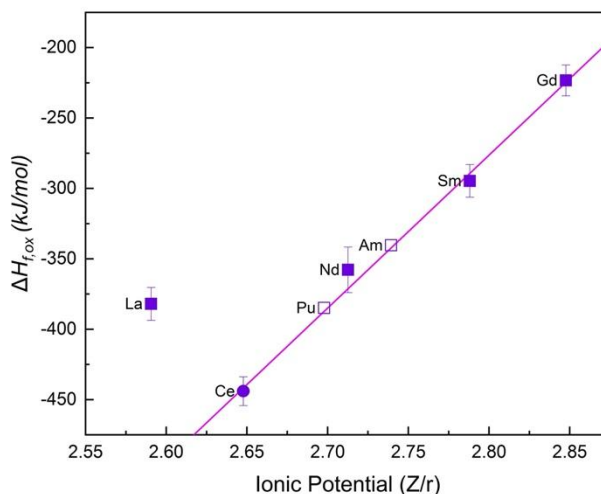


Figure 10. Variation of the enthalpies of formation of $\text{RE}_{4.67}(\text{SiO}_4)_3\text{O}$ from the oxides ($\Delta H_{f, \text{ox}}$) versus the ionic potential of Ln^{3+} cation ion. The equation describing the line is $\Delta H_{f, \text{ox}} \text{ (kJ/mol)} = (-3374.4 \pm 102.6) + (1106.3 \pm 38.2) \cdot (Z/r)$, with an adjusted $R^2 = 0.996$. Data reported for La, Nd, Sm, and Gd were extracted from Risbud *et al.* (2001)²³ while data associated to Pu and Am were evaluated from the fitted equation of the line and the known ionic radii in the 7-fold and 9-fold coordination environments.^{68,117}

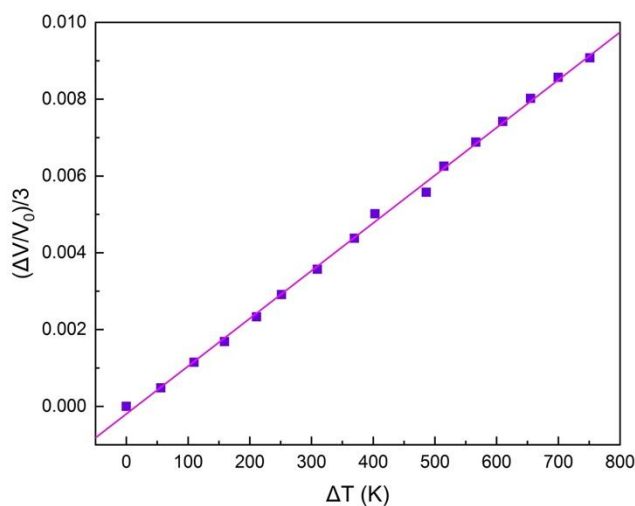


Figure 11. Variation of $(\Delta V/V_0)/3$ values versus ΔT obtained for the $\text{A-Ce}_2\text{Si}_2\text{O}_7$. The equation of the line describing the linear fitting is $(\Delta V/V_0)/3 = (-1.9604 \pm 0.5800) \times 10^{-4} + (1.2425 \pm 0.0130) \times 10^{-5} \cdot \Delta T$, with an adjusted $R^2 = 0.998$.

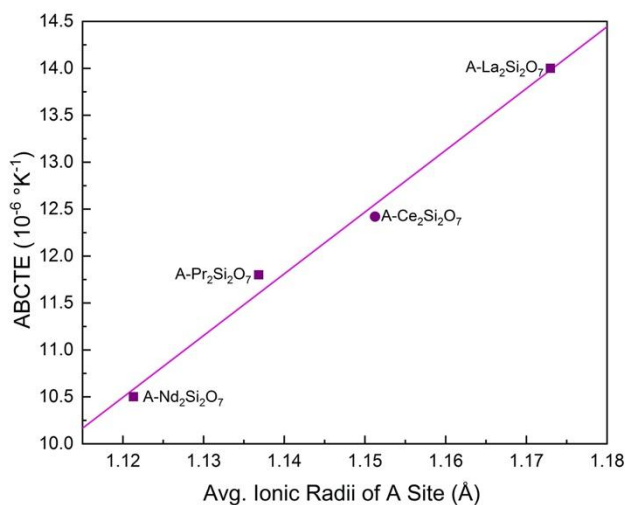


Figure 12. Comparison of ABCTE values of isostructural A-RE₂Si₂O₇ versus the average ionic size of the A site metal cation. Values reported as *squares* were extracted from Fernández-Carrión *et al.*¹, while the value pointed as a *circle* is from this study. The equation of the line describing the linear trend is $\text{ABCTE} (10^{-6} \text{ K}^{-1}) = (-63.2 \pm 5.3) + (65.8 \pm 4.7) \cdot r$, with an adjusted $R^2 = 0.985$. The A-RE₂Si₂O₇ unit cell belongs to the $P4_1$ space group which exhibits four different crystallographic sites for the RE³⁺. These four sites differ in coordination with having coordination numbers of 7, 8, 9, and 9. For this reason averaging was done through taking the reported ionic size⁶⁸ of the RE³⁺ cation in the four coordination environments, values reported in Table 6.

ASSOCIATED CONTENT

The Supporting Information is available: PXRD, thermodynamic data, and thermochemical tables.

References:

- (1) Fernández-Carrión, A. J.; Allix, M.; Becerro, A. I. Thermal Expansion of Rare-Earth Pyrosilicates. *J. Am. Ceram. Soc.* **2013**, 96 (7), 2298–2305. <https://doi.org/10.1111/jace.12388>.
- (2) Xu, Y.; Hu, X.; Xu, F.; Li, K. Rare Earth Silicate Environmental Barrier Coatings: Present Status and Prospective. *Ceram. Int.* **2017**, 43 (8), 5847–5855. <https://doi.org/10.1016/j.ceramint.2017.01.153>.
- (3) Zhu, D. Aerospace Ceramic Materials: Thermal, Environmental Barrier Coatings and SiC/SiC Ceramic Matrix Composites for Turbine Engine Applications; **2018**.
- (4) Lee, K. N.; Fox, D. S.; Bansal, N. P. Rare Earth Silicate Environmental Barrier Coatings for SiC/SiC Composites and Si₃N₄ Ceramics. *J. Eur. Ceram. Soc.* **2005**, 25 (10 SPEC. ISS.), 1705–1715. <https://doi.org/10.1016/j.jeurceramsoc.2004.12.013>.
- (5) Wang, Y. Q.; Huang, J. F.; Cao, L. Y.; Zeng, X. R. Y₂Si₂O₇ Whisker Reinforced MoSi₂ Multi-Composition Coating for SiC Pre-Coated Carbon/Carbon Composites. *Adv. Compos. Mater.* **2011**, 20 (2), 125–132. <https://doi.org/10.1163/092430410X523944>.
- (6) Cao, X. Q.; Vassen, R.; Stoeber, D. Ceramic Materials for Thermal Barrier Coatings. *J. Eur. Ceram. Soc.* **2004**, 24 (1), 1–10. [https://doi.org/10.1016/S0955-2219\(03\)00129-8](https://doi.org/10.1016/S0955-2219(03)00129-8).
- (7) Dolan, M. D.; Harlan, B.; White, J. S.; Hall, M.; Misture, S. T.; Bancheri, S. C.; Bewlay, B. Structures and Anisotropic Thermal Expansion of the α , β , γ , and δ Polymorphs of Y₂Si₂O₇. *Powder Diffr.* **2008**, 23 (1), 20–25. <https://doi.org/10.1154/1.2825308>.
- (8) Fukuda, K.; Matsubara, H. Thermal Expansion of Delta-Yttrium Disilicate Koichiro. *J. Am. Ceram. Soc.* **2004**, 87, 89–92. <https://doi.org/10.1107/97809553602060000903>.
- (9) Aparicio, M.; Durán, A. Yttrium Silicate Coatings for Oxidation Protection of Carbon- Silicon Carbide Composites. *J. Am. Ceram. Soc.* **2004**, 83 (6), 1351–1355. <https://doi.org/10.1111/j.1151-2916.2000.tb01392.x>.
- (10) Costa, G.; Harder, B. J.; Wiesner, V. L.; Jacobson, N. S.; Zhu, D.; Kapush, D.; Bansal, N.; Lee, K. N.; Ushakov, S. V; Navrotsky, A.; et al. Thermodynamics of Reaction between Gas - Turbine Ceramic Coatings and Ingested CMAS Corrodents. *J. Am. Ceram. Soc.* **2018**, 2948–2964. <https://doi.org/10.1111/jace.16113>.
- (11) Costa, G.; Harder, B. J.; Bansal, N. P.; Kowalski, B. A.; Stokes, J. L. Thermochemistry of Calcium Rare-Earth Silicate Oxyapatites. *J. Am. Ceram. Soc.* **2020**, 103 (2), 1446–1453. <https://doi.org/10.1111/jace.16816>.

- (12) Webster, R. I.; Bansal, N. P.; Salem, J. A.; Opila, E. J.; Wiesner, V. L. Characterization of Thermochemical and Thermomechanical Properties of Eyjafjallajökull Volcanic Ash Glass. *Coatings* **2020**, 10 (2), 1–20.
- (13) Poerschke, D. L.; Jackson, R. W.; Levi, C. G. Silicate Deposit Degradation of Engineered Coatings in Gas Turbines : Progress Toward Models and Materials Solutions. *Annu. Rev. Mater. Res.* **2017**, 47 (1), 297–330.
- (14) Felsche, J. Polymorphism and Crystal Data of the Rare-Earth Disilicates of Type R.E.₂Si₂O₇. *J. Less-Common Met.* **1970**, 21, 1–14.
- (15) Felsche, J. Rare Earth Silicates with the Apatite Structure. *J. Solid State Chem.* **1972**, 5 (2), 266–275. [https://doi.org/10.1016/0022-4596\(72\)90039-4](https://doi.org/10.1016/0022-4596(72)90039-4).
- (16) Felsche, J.; Hirsiger, W. The Polymorphs of the Rare-Earth Pyrosilicates R.E.₂Si₂O₇, [R.E.: La, Ce, Pr, Nd, Sm]. *J. Less-Common Met.* **1969**, 18 (2), 131–137. [https://doi.org/10.1016/0022-5088\(69\)90132-5](https://doi.org/10.1016/0022-5088(69)90132-5).
- (17) Zec, S.; Boskovic, S. Cerium Silicates Formation from Mechanically Activated Oxide Mixtures. *J. Mater. Sci.* **2004**, 39 (16–17), 5283–5286. <https://doi.org/10.1023/B:JMISC.0000039229.35551.9e>.
- (18) Kępiński, L.; Wołczyrz, M.; Marchewka, M. Structure Evolution of Nanocrystalline CeO₂ Supported on Silica: Effect of Temperature and Atmosphere. *J. Solid State Chem.* **2002**, 168 (1), 110–118. <https://doi.org/10.1006/jssc.2002.9697>.
- (19) Kępiński, L.; Hreniak, D.; Stręk, W. Microstructure and Luminescence Properties of Nanocrystalline Cerium Silicates. *J. Alloys Compd.* **2002**, 341 (1–2), 203–207. [https://doi.org/10.1016/S0925-8388\(02\)00077-4](https://doi.org/10.1016/S0925-8388(02)00077-4).
- (20) Marageh, M. G.; Husain, S. W.; Khanchi, A. R.; Ahmady, S. J. Sorption Studies of Radionuclides on a New Ion Exchanger: Cerium (III) Silicate. *Appl. Radiat. Isot.* **1996**, 47 (5–6), 501–505. [https://doi.org/10.1016/0969-8043\(95\)00322-3](https://doi.org/10.1016/0969-8043(95)00322-3).
- (21) Felsche, J. The Crystal Chemistry of the Rare-Earth Silicates. In *Structure and Bonding: Rare Earths*; Springer Berlin Heidelberg: Berlin, **1973**; pp 99–197. https://doi.org/10.1007/3-540-06125-8_3.
- (22) Ayyasamy, M. V.; Deijkers, J. A.; Wadley, H. N. G.; Balachandran, P. V. Density Functional Theory and Machine Learning Guided Search for RE₂Si₂O₇ with Targeted Coefficient of Thermal Expansion. *J. Am. Ceram. Soc.* **2020**, No. January, 1–9. <https://doi.org/10.1111/jace.17121>.
- (23) Risbud, A. S.; Helean, K. B.; Wilding, M. C.; Lu, P.; Navrotsky, A. Enthalpies of Formation of Lanthanide Oxyapatite Phases. *J. Mater. Res.* **2001**, 16 (10), 2780–2783. <https://doi.org/10.1557/JMR.2001.0381>.

- (24) Fukuda, K.; Asaka, T.; Uchida, T. Thermal Expansion of Lanthanum Silicate Oxyapatite ($\text{La}_{9.332x}(\text{SiO}_4)_6\text{O}_{23x}$), Lanthanum Oxyorthosilicate (La_2SiO_5) and Lanthanum Sorosilicate ($\text{La}_2\text{Si}_2\text{O}_7$). *J. Solid State Chem.* **2012**, 194, 157–161. <https://doi.org/10.1016/j.jssc.2012.04.043>.
- (25) Cordfunke, E. H. P.; Booij, A. S.; Van Der Laan, R. R. The Thermochemical Properties of $\text{Y}_2\text{Si}_2\text{O}_7$ and $\text{Dy}_2\text{Si}_2\text{O}_7$. *J. Chem. Thermodyn.* **1998**, 30, 199–205.
- (26) Tas, A. C.; Akinc, M. Cerium Oxygen Apatite ($\text{Ce}_{4.67}[\text{SiO}_4]_3\text{O}$) X-Ray Diffraction Pattern Revisited. *Powder Diffr.* 1992, 7 (4), 219–222. <https://doi.org/10.1017/S0885715600018753>.
- (27) Tas, A. C.; Akinc, M. Phase Relations in the System Ce_2O_3 – $\text{Ce}_2\text{Si}_2\text{O}_7$ in the Temperature Range 1150° to 1970°C in Reducing and Inert Atmospheres. *J. Am. Ceram. Soc.* **1994**, 77 (11), 2953–2960. <https://doi.org/10.1111/j.1151-2916.1994.tb04530.x>.
- (28) Bunzli, J.-C. G.; McGill, I. Rare Earth Elements; **2018**. <https://doi.org/10.1007/978-3-642-35458-8>.
- (29) Zamoryanskaya, M. V.; Burakov, B. E. Feasibility Limits in Using Cerium as a Surrogate for Plutonium Incorporation in Zircon, Zirconia and Pyrochlore. *Mater. Res. Soc. Symp. - Proc.* **2001**, 663, 301–306. <https://doi.org/10.1557/proc-663-301>.
- (30) Putnam, R. L.; Navrotsky, A.; Cordfunke, E. H. P.; Huntelaar, M. E. Thermodynamics of Formation of Two Cerium Aluminum Oxides, $\text{CeAlO}_{3(s)}$ and $\text{CeAl}_{12\text{O}19.918(s)}$, and Cerium Sesquioxide, $\text{Ce}_2\text{O}_{3(s)}$ At $T = 298.15$ K. *J. Chem. Thermodyn.* **2000**, 32 (7), 911–921. <https://doi.org/10.1006/jcht.2000.0665>.
- (31) Putnam, R. L.; Gallegos, U. F.; Ebbinghaus, B. B.; Navrotsky, A.; Helean, K. B.; Ushakov, S. V.; Woodfield, B. F.; Boerio-Goates, J.; Williamson, M. A. Formation Energetics of Ceramic Phases Related to Surplus Plutonium Disposition; Los Alamos, **2000**.
- (32) Marra, J. C.; Cozzi, A. D.; Pierce, R. A.; Pareizs, J. M.; Jurgensen, A. R.; Missimer, D. M. Cerium as a Surrogate in the Plutonium Immobilized Form. In *Environmental Issues and Waste Management Technologies in the Ceramic and Nuclear Industries*; Smith, G. L., Sundaram, S. K., Spearing, D. R., Eds.; *American Ceramic Society*, **2002**; pp 381–388.
- (33) Strzelecki, A. C.; Bourgeois, C.; Kriegsman, K. W.; Zhao, X.; Estevenon, P.; Wei, N.; Szenknect, S.; Mesbah, A.; Wu, D.; Ewing, R. C.; Dacheux, N.; Guo, X. Thermodynamics of CeSiO_4 : Implications for Actinide Orthosilicates. *Inorg. Chem.* **2020**. (*in press*). <https://doi.org/10.1021/acs.inorgchem.0c01476>.
- (34) Holtstam, D.; Norrestam, R.; Andersson, U. B. Percleveite-(Ce)- A New Lanthanide Disilicate Mineral from Bastnäs, Skinnskatteberg, Sweden. *Eur. J. Mineral.* **2003**, 15 (4), 725–731. <https://doi.org/10.1127/0935-1221/2003/0015-0725>.
- (35) Li, Y.; Zhang, T.; Liu, C.; Jiang, M. Thermodynamic and Experimental Studies on Al Addition of 253MA Steel. *Metals* (Basel). **2019**, 9 (4), 1–7. <https://doi.org/10.3390/met9040433>.

- (36) Schlüter, J.; Malcherek, T.; Husdal, T. A. The New Mineral Stetindite, CeSiO_4 , a Cerium End-Member of the Zircon Group. *Neues Jahrb. für Mineral. Abhandlungen* **2009**, 186 (2), 195–200. <https://doi.org/10.1127/0077-7757/2009/0146>.
- (37) Estevenon, P.; Kaczmarek, T.; Vadot, F.; Dumas, T.; Solari, P. L.; Welcomme, E.; Szenknect, S.; Mesbah, A.; Moisy, P.; Poinssot, C.; Dacheux, N.; Formation of CeSiO_4 from Cerium (III) Silicate Precursors. *Dalt. Trans.* **2019**, 48, 10455–10463. <https://doi.org/10.1039/c9dt01990a>.
- (38) Estevenon, P.; Welcomme, E.; Tamain, C.; Jouan, G.; Szenknect, S.; Mesbah, A.; Poinssot, C.; Moisy, P.; Dacheux, N. Formation of PuSiO_4 under Hydrothermal Conditions. *Dalt. Trans.* **2020**. <https://doi.org/https://doi.org/10.1039/D0DT01183E>.
- (39) Buscheck, T. A.; Glascoe, L. G.; Lee, K. H.; Gansemer, J.; Sun, Y.; Mansoor, K. Validation of the Multiscale Thermohydrologic Model Used for Analysis of a Proposed Repository at Yucca Mountain. *J. Contam. Hydrol.* **2003**, 62–63, 421–440. [https://doi.org/10.1016/S0169-7722\(02\)00157-2](https://doi.org/10.1016/S0169-7722(02)00157-2).
- (40) Haukwa, C. B.; Wu, Y. S.; Bodvarsson, G. S. Modeling Thermal-Hydrological Response of the Unsaturated Zone at Yucca Mountain, Nevada, to Thermal Load at a Potential Repository. *J. Contam. Hydrol.* **2003**, 62–63, 529–552. [https://doi.org/10.1016/S0169-7722\(02\)00188-2](https://doi.org/10.1016/S0169-7722(02)00188-2).
- (41) Löfman, J. Simulation of Hydraulic Disturbances Caused by the Decay Heat of the Repository in Olkiluoto Simulation of Hydraulic Disturbances Caused by the Decay Heat of the Repository in Olkiluoto; OLKILUOTO, **2005**.
- (42) Zhou, W.; Apted, M. J.; Kessler, J. H. The Thermal-Hydrological Impact on Increased Spent-Fuel Storage Capacity in Yucca Mountain Repository. *Nucl. Technol.* **2010**, 170 (2), 336–352. <https://doi.org/10.13182/NT10-A9487>.
- (43) Blanco Martín, L.; Rutqvist, J.; Birkholzer, J. T. Long-Term Modeling of the Thermal-Hydraulic-Mechanical Response of a Generic Salt Repository for Heat-Generating Nuclear Waste. *Eng. Geol.* **2015**, 193, 198–211. <https://doi.org/10.1016/j.enggeo.2015.04.014>.
- (44) Winter, J. D. Principles of Igneous and Metamorphic Petrology, 2nd ed.; Pearson, **2013**.
- (45) Estevenon, P.; Causse, J.; Szenknect, S.; Welcomme, E.; Mesbah, A.; Moisy, P.; Poinssot, C.; Dacheux, N. In-Situ Study of the Synthesis of Thorite (ThSiO_4) under Environmental Representative Conditions. *Dalt. Trans.* **2020**, 1–11. <https://doi.org/10.1039/D0DT01790F>.
- (46) Neill, T. S.; Morris, K.; Pearce, C. I.; Sherriff, N. K.; Burke, M. G.; Chater, P. A.; Janssen, A.; Natrajan, L.; Shaw, S. Stability, Composition, and Core-Shell Particle Structure of Uranium(IV)-Silicate Colloids. *Environ. Sci. Technol.* **2018**, 52 (16), 9118–9127. <https://doi.org/10.1021/acs.est.8b01756>.
- (47) Hennig, C.; Weiss, S.; Banerjee, D.; Brendler, E.; Honkimäki, V.; Cuello, G.; Ikeda-Ohno, A.; Scheinost, A. C.; Zänker, H. Solid-State Properties and Colloidal Stability of Thorium(IV)-Silica

- Nanoparticles. *Geochim. Cosmochim. Acta* **2013**, 103, 197–212.
<https://doi.org/10.1016/j.gca.2012.10.051>.
- (48) Zänker, H.; Weiss, S.; Hennig, C.; Brendler, V.; Ikeda-Ohno, A. Oxyhydroxy Silicate Colloids: A New Type of Waterborne Actinide(IV) Colloids. *ChemistryOpen* **2016**, 5 (3), 174–182.
<https://doi.org/10.1002/open.201500207>.
- (49) Estevenon, P.; Welcomme, E.; Szenknect, S.; Mesbah, A.; Moisy, P.; Poinssot, C.; Dacheux, N. Multiparametric Study of the Synthesis of ThSiO₄ under Hydrothermal Conditions. *Inorg. Chem.* **2018**, 57 (15), 9393–9402. <https://doi.org/10.1021/acs.inorgchem.8b01390>.
- (50) Szenknect, S.; Mesbah, A.; Cordara, T.; Clavier, N.; Brau, H. P.; Le Goff, X.; Poinssot, C.; Ewing, R. C.; Dacheux, N. First Experimental Determination of the Solubility Constant of Coffinite. *Geochim. Cosmochim. Acta* **2016**, 181, 36–53. <https://doi.org/10.1016/j.gca.2016.02.010>.
- (51) Altmaier, M.; Gaona, X.; Fanghänel, T. Recent Advances in Aqueous Actinide Chemistry and Thermodynamics. *Chem. Rev.* **2013**, 113 (2), 901–943. <https://doi.org/10.1021/cr300379w>.
- (52) Wheaton, V.; Majumdar, D.; Balasubramanian, K.; Chauffe, L.; Allen, P. G. A Comparative Theoretical Study of Uranyl Silicate Complexes. *Chem. Phys. Lett.* **2003**, 371 (3–4), 349–359.
[https://doi.org/10.1016/S0009-2614\(03\)00237-9](https://doi.org/10.1016/S0009-2614(03)00237-9).
- (53) Novikov, A. P.; Kalmykov, S. N.; Utsunomiya, S.; Ewing, R. C.; Horreard, F.; Merkulov, A.; Clark, S. B.; Tkachev, V. V.; Myasoedov, B. F. Colloid Transport of Plutonium in the Far-Field of the Mayak Production Association, Russia. *Science* (80-.). 2006, 314 (5799), 638–641.
<https://doi.org/10.1126/science.1131307>.
- (54) Utsunomiya, S.; Kersting, A. B.; Ewing, R. C. Groundwater Nanoparticles in the Far-Field at the Nevada Test Site: Mechanism for Radionuclide Transport. *Environ. Sci. Technol.* **2009**, 43 (5), 1293–1298. <https://doi.org/10.1021/es802181t>.
- (55) Dittrich, T. M.; Boukhalfa, H.; Ware, S. D.; Reimus, P. W. Laboratory Investigation of the Role of Desorption Kinetics on Americium Transport Associated with Bentonite Colloids. *J. Environ. Radioact.* **2015**, 148, 170–182. <https://doi.org/10.1016/j.jenvrad.2015.07.001>.
- (56) Prescher, C.; Prakapenka, V. B. DIOPTAS: A Program for Reduction of Two-Dimensional X-Ray Diffraction Data and Data Exploration. *High Press. Res.* **2015**, 35 (3), 223–230.
<https://doi.org/10.1080/08957959.2015.1059835>.
- (57) Toby, B. H.; Von Dreele, R. B. GSAS-II: The Genesis of a Modern Open-Source All Purpose Crystallography Software Package. *J. Appl. Crystallogr.* **2013**, 46 (2), 544–549.
<https://doi.org/10.1107/S0021889813003531>.
- (58) Deng, B.; Ibers, J. A. Dicerium Disilicate, Ce₂[Si₂O₇]. *Acta Crystallogr. Sect. E Struct. Reports Online* **2005**, 61 (5), 76–78. <https://doi.org/10.1107/S1600536805011049>.

- (59) Belokoneva, E. L.; Petrova, T. L.; Simonov, M. A.; Belov, N. V. Crystal-Structure of Synthetic TR-Analogs of Apatite $\text{Dy}_{4.67}(\text{GeO}_4)_3\text{O}$ and $\text{Ce}_{4.67}(\text{SiO}_4)_3\text{O}$. *Kristallografiya* **1972**, 17 (3), 429–431.
- (60) Navrotsky, A. Progress and New Directions in Calorimetry: A 2014 Perspective. *J. Am. Ceram. Soc.* **2014**, 97 (11), 3349–3359. <https://doi.org/10.1111/jace.13278>.
- (61) Guo, X.; Szenknect, S.; Mesbah, A.; Labs, S.; Clavier, N.; Poinssot, C.; Ushakov, S. V.; Curtius, H.; Bosbach, D.; Ewing, R. C.; et al. Thermodynamics of Formation of Coffinite, USiO_4 . *Proc. Natl. Acad. Sci.* **2015**, 112 (21), 6551–6555. <https://doi.org/10.1073/pnas.1507441112>.
- (62) Helean, K. B.; Navrotsky, A.; Vance, E. R.; Carter, M. L.; Ebbinghaus, B.; Krikorian, O.; Lian, J.; Wang, L. M.; Catalano, J. G. Enthalpies of Formation of Ce-Pyrochlore, $\text{Ca}_{0.93}\text{Ce}_{1.00}\text{Ti}_{2.035}\text{O}_{7.00}$, U-Pyrochlore, $\text{Ca}_{1.46}\text{U}^{4+}_{0.23}\text{U}^{6+}_{0.46}\text{Ti}_{1.85}\text{O}_{7.00}$ and Gd-Pyrochlore, $\text{Gd}_2\text{Ti}_2\text{O}_7$: Three Materials Relevant to the Proposed Waste Form for Excess Weapons Plutonium. *J. Nucl. Mater.* **2002**, 303 (2–3), 226–239. [https://doi.org/10.1016/s0022-3115\(02\)00795-x](https://doi.org/10.1016/s0022-3115(02)00795-x).
- (63) Navrotsky, A.; Shvareva, T.; Guo, X. Thermodynamics of Uranium Minerals and Related Materials. In Mineralogical Association of Canada Short Course 43; **2013**; pp 1–18.
- (64) Guo, X.; Tiferet, E.; Qi, L.; Solomon, J. M.; Lanzirrotti, A.; Newville, M.; Engelhard, M. H.; Kukkadapu, R. K.; Wu, D.; Ilton, E. S.; et al. U(v) in Metal Uranates: A Combined Experimental and Theoretical Study of MgUO_4 , CrUO_4 , and FeUO_4 . *Dalt. Trans.* **2016**, 45 (11), 4622–4632. <https://doi.org/10.1039/c6dt00066e>.
- (65) Guo, X.; Wu, D.; Xu, H.; Burns, P. C.; Navrotsky, A. Thermodynamic Studies of Studtite Thermal Decomposition Pathways via Amorphous Intermediates UO_3 , U_2O_7 , and UO_4 . *J. Nucl. Mater.* **2016**, 478, 158–163. <https://doi.org/10.1016/j.jnucmat.2016.06.014>.
- (66) Gorman-Lewis, D.; Mazeina, L.; Fein, J. B.; Szymanowski, J. E. S.; Burns, P. C.; Navrotsky, A. Thermodynamic Properties of Soddyite from Solubility and Calorimetry Measurements. *J. Chem. Thermodyn.* **2007**, 39 (4), 568–575. <https://doi.org/10.1016/j.jct.2006.09.005>.
- (67) Bolech, M.; Janssen, F. J. J. G.; Booij, A. S.; Cordfunke, E. H. P. The Standard Molar Enthalpies of Formation of $\beta\text{-La}_2\text{Si}_2\text{O}_7$ and $\beta\text{-Ce}_2\text{Si}_2\text{O}_7$. *J. Chem. Thermodyn.* **1996**, 28 (11), 1319–1324. <https://doi.org/10.1006/jcht.1996.0116>.
- (68) Shannon, R. D. Revised Effective Ionic Radii and Systematic Studies of Interatomic Distances in Halides and Chalcogenides. *Acta Crystallogr. Sect. A* **1976**, 32 (5), 751–766. <https://doi.org/10.1107/S0567739476001563>.
- (69) Hosseini, S. M.; Navrotsky, A. Energetic Effects of Substitution of La-Nd and Si-Ge Oxyapatite-Type Materials. *J. Am. Ceram. Soc.* **2013**, 96 (12), 3915–3919. <https://doi.org/10.1111/jace.12705>.
- (70) Hosseini, S. M.; Shvareva, T.; Navrotsky, A. Energetics of Lanthanum Silicate Apatite: Influence of Interstitial Oxygen and Cation Vacancy Concentrations in $\text{La}_{9.33+x}(\text{SiO}_4)_6\text{O}_{2+3x/2}$ and $\text{La}_{10-x}\text{Sr}_x(\text{SiO}_4)_6\text{O}_{3-0.5x}$. *Solid State Ionics* **2013**, 233, 62–66. <https://doi.org/10.1016/j.ssi.2012.12.012>.

- (71) Ueno, S.; Jayaseelan, D. D.; Kita, H.; Ohji, T.; Lin, H. T. Comparison of Water Vapor Corrosion Behaviors of $\text{Ln}_2\text{Si}_2\text{O}_7$ (Ln=Yb and Lu) and ASiO_4 (A=Ti, Zr and Hf) EBC's. *Key Eng. Mater.* **2006**, 317–318, 557–560. <https://doi.org/10.4028/www.scientific.net/kem.317-318.557>.
- (72) Garcia, E.; Trapaga, G.; Sampath, S. Characterization of $\text{Yb}_2\text{Si}_2\text{O}_7$ – Yb_2SiO_5 Composite Environmental Barrier Coatings Resultant from in Situ Plasma Spray Processing. *Ceram. Int.* **2020**. <https://doi.org/10.1016/j.ceramint.2020.05.228>.
- (73) Ding, Z.; Ridley, M.; Deijkers, J.; Liu, N.; Hoque, M. S. Bin; Gaskins, J.; Zebarjadi, M.; Hopkins, P.; Wadley, H.; Opila, E.; Esfarjani, K.; The Physical and Mechanical Properties of Hafnium Orthosilicate: Experiments and First-Principles Calculations. *Preprint* **2020**.
- (74) Nesse, W. D. Introduction to Mineralogy, 2nd ed.; Oxford University Press, **2000**.
- (75) West, A. Solid State Chemistry and Its Application; **2003**. <https://doi.org/10.1016/B978-0-444-51436-3.X5000-7>.
- (76) Klemm, H. Silicon Nitride for High-Temperature Applications. *J. Am. Ceram. Soc.* **2010**, 93 (6), 1501–1522. <https://doi.org/10.1111/j.1551-2916.2010.03839.x>.
- (77) Navrotsky, A. Systematic Trends and Prediction of Enthalpies of Formation of Refractory Lanthanide and Actinide Ternary Oxide Phases. *Ceram. Trans.* **2001**, No. 119, 137–146.
- (78) Helean, K. B.; Navrotsky, A.; Lumpkin, G. R.; Colella, M.; Lian, J.; Ewing, R. C.; Ebbinghaus, B.; Catalano, J. G. Enthalpies of Formation of U-, Th-, Ce-Brannerite: Implications for Plutonium Immobilization. *J. Nucl. Mater.* **2003**, 320 (3), 231–244. [https://doi.org/10.1016/S0022-3115\(03\)00186-7](https://doi.org/10.1016/S0022-3115(03)00186-7).
- (79) Navrotsky, A. Thermochemical Insights into Refractory Ceramic Materials Based on Oxides with Large Tetravalent Cations. *J. Mater. Chem.* **2005**, 15 (19), 1883–1890. <https://doi.org/10.1039/b417143h>.
- (80) Qi, J.; Guo, X.; Mielewczyk-Gryn, A.; Navrotsky, A. Formation Enthalpies of LaLnO_3 (Ln=Ho, Er, Tm and Yb) Interlanthanide Perovskites. *J. Solid State Chem.* **2015**, 227, 150–154. <https://doi.org/10.1016/j.jssc.2015.03.026>.
- (81) Helean, K. B.; Ushakov, S. V.; Brown, C. E.; Navrotsky, A.; Lian, J.; Ewing, R. C.; Farmer, J. M.; Boatner, L. A. Formation Enthalpies of Rare Earth Titanate Pyrochlores. *J. Solid State Chem.* **2004**, 177 (6), 1858–1866. <https://doi.org/10.1016/j.jssc.2004.01.009>.
- (82) Chen, F.; Ewing, R. C.; Clark, S. B. The Gibbs Free Energies and Enthalpies of Formation of U^{6+} Phases: An Empirical Method of Prediction. *Am. Mineral.* **1999**, 84 (4), 650–664. <https://doi.org/10.2138/am-1999-0418>.
- (83) Sverjensky, D.; Shock, E. L.; Helgeson, H. C. Prediction of the Thermodynamic Properties of Aqueous Metal Complexes to 1000 C and 5 Kb. *Geochim. Cosmochim. Acta* **1997**, 61 (7), 1359–1412. [https://doi.org/10.1016/S0016-7037\(97\)00009-4](https://doi.org/10.1016/S0016-7037(97)00009-4).

- (84) Jenkins, H. D. B.; Glasser, L. Standard Absolute Entropy, S°_{298} , Values from Volume or Density. *Inorg. Chem.* **2003**, 42 (26), 8702–8708. <https://doi.org/10.1021/ic030219p>.
- (85) Anderson, D. L.; Anderson, O. L. The Bulk Modulus-Volume Relationship for Oxides. *J. Geophys. Res.* **1970**, 75 (17), 3494–3500.
- (86) Xu, H.; Zhao, Y.; Zhang, J.; Wang, Y.; Hickmott, D. D.; Daemen, L. L.; Hartl, M. A.; Wang, L. Anisotropic Elasticity of Jarosite: A High-P Synchrotron XRD Study. *Am. Mineral.* **2009**, 95 (1), 19–23. <https://doi.org/10.2138/am.2010.3280>.
- (87) Glasser, L. Thermodynamics of Condensed Phases: Formula Unit Volume, V_m , and the Determination of the Number of Formula Units, Z , in a Crystallographic Unit Cell. *J. Chem. Educ.* **2011**, 88 (5), 581–585. <https://doi.org/10.1021/ed900046k>.
- (88) Robie, Richard A.; Hemingway, B. S. Thermodynamic Properties of Minerals and Related Substances at 298.15 K and 1 Bar (105 Pascals) Pressure and at Higher Temperatures. *U.S. Geol. Surv. Bull.* **1995**, 2131.
- (89) Strzelecki, A. C.; Barral, T.; Mesbah, A.; Goncharov, V.; Baker, J.; Bai, J.; Estevenon, P.; Szenknect, S.; Migdisov, A. A.; Xu, H.; Ewing R.C.; Dacheux, N.; Guo, X. Role of Water and Hydroxyl Groups in the Structures of Stetindite and Coffinite, $MSiO_4$ (M= Ce, U). *Chem. Mater.* **2020**, Submitted.
- (90) Guo, X.; Xu, H. Enthalpies of Formation of Polyhalite: A Mineral Relevant to Salt Repository. *J. Chem. Thermodyn.* **2017**, 114, 44–47. <https://doi.org/10.1016/j.jct.2017.05.031>.
- (91) Leitner, J.; Sedmidubsky, D.; Ruzicka, K.; Svobo, P. Calorimetric Determination of Heat Capacity, Entropy and Enthalpy of Mixed Oxides in the System $CaO-SrO-Bi_2O_3-Nb_2O_5-Ta_2O_5$. In Applications of Calorimetry in a Wide Context - Differential Scanning Calorimetry, Isothermal Titration Calorimetry and Microcalorimetry; Elkordy, A. A., Ed.; BoD – Books on Demand, **2013**; pp 385–406. <https://doi.org/10.5772/54064>.
- (92) Bolech, M.; Cordfunke, E. H. P.; van Genderen, A. C. G.; Van Der Laan, R. R.; Janssen, F. J. J. G.; van Miltenburg, J. C. The Heat Capacity and Derived Thermodynamic Functions of $La_2Si_2O_7$ and $Ce_2Si_2O_7$ from 4 to 1000 K. *Thermochim. Acta* **1996**, 284 (96), 253–261.
- (93) Ahlborg, N. L.; Zhu, D. Calcium-Magnesium Aluminosilicate (CMAS) Reactions and Degradation Mechanisms of Advanced Environmental Barrier Coatings. *Surf. Coatings Technol.* **2013**, 237, 79–87. <https://doi.org/10.1016/j.surfcoat.2013.08.036>.
- (94) Costin, D. T.; Mesbah, A.; Clavier, N.; Dacheux, N.; Poinssot, C.; Szenknect, S.; Ravaux, J. How to Explain the Difficulties in the Coffinite Synthesis from the Study of Uranothorite? *Inorg. Chem.* **2011**, 50 (21), 11117–11126. <https://doi.org/10.1021/ic2016758>.

- (95) Guo, X.; Szenknect, S.; Mesbah, A.; Clavier, N.; Poinssot, C.; Wu, D.; Xu, H.; Dacheux, N.; Ewing, R. C.; Navrotsky, A. Energetics of a Uranothorite ($\text{Th}_{1-x}\text{U}_x\text{SiO}_4$) Solid Solution. *Chem. Mater.* **2016**, 28 (19), 7117–7124. <https://doi.org/10.1021/acs.chemmater.6b03346>.
- (96) Costin, D. T.; Mesbah, A.; Clavier, N.; Szenknect, S.; Dacheux, N.; Poinssot, C.; Ravau, J.; Brau, H. P. Preparation and Characterization of Synthetic $\text{Th}_{0.5}\text{U}_{0.5}\text{SiO}_4$ Uranothorite. *Prog. Nucl. Energy* **2012**, 57, 155–160. <https://doi.org/10.1016/j.pnucene.2011.10.004>.
- (97) Anderson, G. M.; Crerar, D. A. Thermodynamics in Geochemistry: The Equilibrium Model; Oxford University Press: New York, **1993**.
- (98) Miyawaki, R.; Yokoyama, K.; Husdal, T. A. Bastnäsite-(Nd), a New Nd-Dominant Member of the Bastnäsite Group from the Stetind Pegmatite, Tysfjord, Nordland, Norway. *Eur. J. Mineral.* **2013**, 25 (2), 187–191. <https://doi.org/10.1127/0935-1221/2013/0025-2265>.
- (99) Estevenon, P.; Welcomme, E.; Szenknect, S.; Mesbah, A.; Moisy, P.; Poinssot, C.; Dacheux, N. Preparation of CeSiO_4 from Aqueous Precursors under Soft Hydrothermal Conditions. *Dalt. Trans.* **2019**, 48 (22), 7551–7559. <https://doi.org/10.1039/c9dt01258c>.
- (100) Taylor, S. R.; McLennan, S. M. The Geochemical Evolution of the Continental Crust. *Am. Geophys. Union* **1995**, 33 (2), 241–265.
- (101) Wedepohl, K. H. The Composition of the Continental Crust. *Geochim. Cosmochim. Acta* **1995**, 59 (7), 1217–1232. [https://doi.org/10.1016/0016-7037\(95\)00038-2](https://doi.org/10.1016/0016-7037(95)00038-2).
- (102) Holtstam, D.; Andersson, U. B. The Ree Minerals Of The Bastnäs-Type Deposits, South-Central Sweden. *Can. Mineral.* **2007**, 45, 1073–1114.
- (103) Geijer, P. The Cerium Minerals of Bastnas at Riddarhyttan. *Sveriges Geol. Unders.* **1921**, 1–24.
- (104) Lahti, S. I.; Suominen, V. Occurrence, Crystallography and Chemistry of the Fluocerite-Bastnaesite-Cerianite Intergrowth from the Fjälskär Granite, Southwestern Finland. *Bull. Geol. Soc. Finl.* **2017**, 60 (1), 45–53. <https://doi.org/10.17741/bgsf/60.1.003>.
- (105) Beukes, G. J.; De Bruijn, H.; Van Der Westhuizen, W. A. Fluocerite and Associated Minerals from the Baviaanskranz Granite Pegmatite near Kakamas, South Africa. *South African J. Geol.* **1991**, 94 (4), 313–320.
- (106) Chen, H.; Marcial, J.; Ahmadzadeh, M.; Patil, D.; McCloy, J. Partitioning of Rare Earths in Multiphase Nuclear Waste Glass-Ceramics. *Int. J. Appl. Glas. Sci.* **2020**, No. May, 1–16. <https://doi.org/10.1111/ijag.15726>.
- (107) Urso, K.; Sridharan, K.; Jaques, B. J.; Alanko, G.; Butt, D. P.; Meyer, M.; Xu, P.; Tyburska-Püschel, B. High-Temperature Corrosion Testing of Uranium Silicide Surrogates. *Nucl. Technol.* **2016**, 196 (1), 100–110. <https://doi.org/10.13182/NT15-155>.
- (108) Swift, P. N.; Bonano, E. J. Geological Disposal of Nuclear Waste in Tuff: Yucca Mountain (USA). *Elements* **2016**, 12 (4), 263–268. <https://doi.org/10.2113/gselements.12.4.263>.

- (109) Hedin, A.; Olsson, O. Crystalline Rock as a Repository for Swedish Spent Nuclear Fuel. *Elements* **2016**, 12 (4), 247–252. <https://doi.org/10.2113/gselements.12.4.247>.
- (110) Grambow, B. Geological Disposal of Radioactive Waste in Clay. *Elements* **2016**, 12 (4), 239–245. <https://doi.org/10.2113/gselements.12.4.239>.
- (111) Krumhansl, J. L.; Papenguth, H. W.; Zhang, P. C.; Kelly, J. W.; Anderson, H. L.; Hardesty, J. O. E. Behavior of MgO as a CO₂ Scavenger at the WIPP. *Mater. Res. Soc. Symp. - Proc.* **2000**, 608, 155–160.
- (112) Choppin, G. R. Actinide Speciation in the Environment. *J. Radioanal. Nucl. Chem.* **2007**, 273 (3), 695–703. <https://doi.org/10.1007/s10967-007-0933-3>.
- (113) Cotton, S. Lanthanide and Actinide Chemistry; John Wiley & Sons, Ltd, **2006**.
- (114) Seaborg, G. T. Origin of the Actinide Concept. In Handbook on the Physics and Chemistry of Rare Earths; Gschneidner, K. A., Eyring, L. J., Choppin, G. R., Lander, G. H., Eds.; Elsevier B.V, **1994**; Vol. 18, pp 1–26. [https://doi.org/https://doi.org/10.1016/S0168-1273\(05\)80041-8](https://doi.org/https://doi.org/10.1016/S0168-1273(05)80041-8).
- (115) Seaborg, G. T. The Transuranium Elements. *Nature* **1946**, 104 (2704), 379–386. <https://doi.org/10.1038/159863a0>.
- (116) Momma, K.; Izumi, F. VESTA 3 for Three-Dimensional Visualization of Crystal, Volumetric and Morphology Data. *J. Appl. Crystallogr.* **2011**, 44 (6), 1272–1276. <https://doi.org/10.1107/S0021889811038970>.
- (117) Sawant, R. M.; Verma, P.; Mhatre, H. R.; Chaudhuri, N. K.; Ramakumar, K. L. Stability Constants of the Aqueous Mono-Fluoride Complexes of Pu(III) and Am(III) and Their Correlation with Other Metal Ions. *J. Radioanal. Nucl. Chem.* **2003**, 256 (3), 387–394. <https://doi.org/10.1023/A:1024575010583>.